Tectonophysics 614 (2014) 100–127

Contents lists available at ScienceDirect

Tectonophysics

journal homepage: www.elsevier.com/locate/tecto

Constraints on the dynamics and spatio-temporal evolution of the 2011 Oichalia seismic swarm (SW Peloponnesus, Greece)

I. Kassaras [a,*], V. Kapetanidis [a,b], A. Karakonstantis [a], V. Kouskouna [a], A. Ganas [b], G. Chouliaras [b], G. Drakatos [b], A. Moshou [b], V. Mitropoulou [a], P. Argyrakis [b], E. Lekkas [a], K. Makropoulos [a,b]

[a] Department of Geophysics-Geothermics, University of Athens, 15784 Athens, Greece
[b] Institute of Geodynamics, National Observatory of Athens, Lofos Nymfon, 11810 Athens, Greece

ARTICLE INFO

Article history:
Received 1 April 2013
Received in revised form 14 December 2013
Accepted 22 December 2013
Available online 29 December 2013

Keywords:
Earthquake swarms
Seismic stress
Earthquake source
Spatial analysis
Crustal fluids

ABSTRACT

In this paper, we present a detailed study of a shallow seismic swarm which took place in the area of Oichalia (SW Peloponnesus), between August and December 2011. The seismic crisis started on 14/8/2011 with an $M_w = 4.8$ earthquake and was followed by more than 1600 events, several of which having magnitude over 4.0. The activity was recorded by local temporary and regional permanent seismic stations. Thousands of records were collected and routinely analyzed. P- and S-wave arrival times were manually picked and incorporated in the HYPOINVERSE algorithm together with a new optimum local velocity model. Hypocentral solutions were improved by applying a double-difference method. Focal mechanisms show that the activated fault zone is dominated by dip-slip normal faulting, trending NNW–SSE, with the average T-axes orientation being N70°E, consistent with regional tectonics.

We have investigated towards stress triggering and fluid diffusion, by employing Coulomb stress transfer, spatio-temporal and Frequency–Magnitude Distribution (FMD) analyses. The negligible Coulomb stress transfer and seismicity rate changes that were calculated imply for a stress deficit in the broader study area, hence an external triggering mechanism is required to justify the observed pattern. The *b*-values increase towards the SSE, compatible with the similarly directed migration of seismicity, showed that the Oichalia swarm could possibly be adapted to an Epidemic Type Aftershock Sequence model (ETAS). Fluid diffusion is reflected in the spatio-temporal hypocenter migration. Clustering analysis, combined with the temporal distribution of *b*-values, has shown that the swarm evolved in three major phases, the first two being initiated by major events, which were probably triggered externally due to fluid injection that brought the seismogenic volume into a critical state, likely followed by afterslip. The last phase signified a relaxation period, with dispersed seismicity throughout the area and the *b*-values gently diminishing towards unity.

1. Introduction

The two most important types of earthquake clustering are aftershock sequences and earthquake swarms. The first are associated with a main shock, while the latter occur mainly in volcanic areas, geothermal fields and ocean ridges (e.g. Wyss et al., 1997). Earthquake swarms are typically not characterized by a dominant earthquake. It is uncommon for swarms, not related to active volcanism, to take place in intraplate regions, and when they occur they are often a result of underlying aseismic deformation processes such as intrusion of fluids that reduce the resistance of faults (Kisslinger, 1975; Noir et al., 1997; Yamashita, 1999). Additionally, each event in a swarm is capable to redistribute stress, which in turn influences the subsequent swarm evolution, especially if the crust is in a critical state (Main, 1996), providing a self-triggering mechanism. These processes are in general not directly observable. However, the analysis of the spatio-temporal swarm characteristics, particularly the migration pattern, can remarkably aid to unfold the underlying mechanism.

In this work, we focus on a seismic swarm occurred in 2011 in Oichalia (SW Peloponnesus) and present a high resolution image of its hypocenters and their temporal evolution. The study area is one of the most tectonically and seismically active intraplate areas of the Aegean region (Fig. 1). This is due to its proximity to the Hellenic trench, which is located several tens of km to the west, where the eastern Mediterranean oceanic lithosphere subducts beneath the Aegean microplate (Jackson and McKenzie, 1984; Le Pichon, 1983; McKenzie, 1972; Papazachos et al., 2000) at a rate of about 30 mm/yr (i.e. Nyst and Thatcher, 2004). The convergent plate motion results in intense deformation of the crust and the release of elastic energy by seismic slip along large, roughly N–S trending faults (e.g. Armijo et al., 1992; Pavlides, 1993; Roberts and Ganas, 2000; Taymaz et al., 1990). E–W extensional deformation is reported in the area by seismological data (e.g. Lyon-Caen et al., 1988), tectonics (e.g. Armijo et al., 1992) and

* Corresponding author. Tel.: +30 210 7274792; fax: +30 210 7274787.
E-mail address: kassaras@geol.uoa.gr (I. Kassaras).

0040-1951/$ – see front matter © 2013 Elsevier B.V. All rights reserved.
http://dx.doi.org/10.1016/j.tecto.2013.12.012

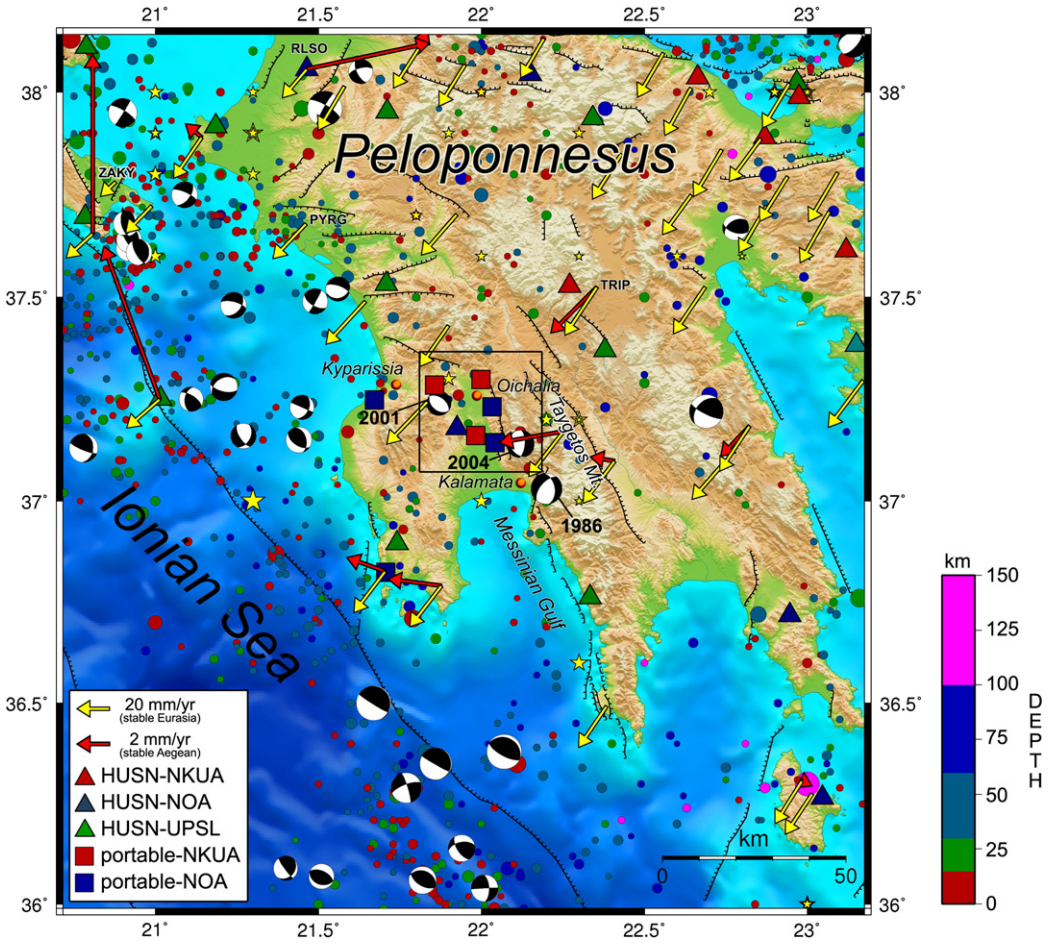

Fig. 1. Seismotectonic map of Peloponnesus. The main tectonic features (continuous lines), are from Armijo et al. (1992) and Lyon-Caen et al. (1988). Barbed lines denote normal faults, while stars represent epicenters of historical earthquakes that occurred before 1900 (Papazachos and Papazachou, 2003). Solid circles are instrumental earthquakes with origin time after the year 1900 ($M_s \geq 4.0$, Makropoulos et al., 2012). Beach-ball diagrams are CMT solutions (1976–2012) for the largest events occurred in the broader area of western Greece ($M_w \geq 5.0$). The size of epicenters and focal mechanisms is proportional to the magnitude. The seismological stations that have been used in this work for earthquake location and tomography studies are represented by solid squares and triangles for temporary and permanent HUSN stations, respectively. The black rectangle indicates the study area. HUSN: Hellenic Unified Seismological Network; NKUA: National and Kapodistrian University of Athens; NOA: National Observatory of Athens; UPSL: University of Patras Seismological Laboratory. Yellow arrows correspond to velocity vectors relative to stable Eurasia calculated from CGPS measurements after Floyd et al. (2010). Red arrows denote velocity vectors relative to a stable Aegean reference frame (Vernant et al., 2014).

GPS observations (McClusky et al., 2000; Vernant et al., 2014). A component of regional uplift is also present due to the 3–5 times higher velocity of the overriding Aegean plate in comparison to the descending plate of eastern Mediterranean (Ganas and Parsons, 2009).

The geology of Messinia is mostly composed of sedimentary rocks of the alpine orogenesis (Fytrolakis, 1971; Mariolakos et al., 1994; Ladas et al., 2004; Fig. 2). The nappe sequence consists of the Tripolis unit and the Pindos unit. The Tripolis unit is composed of neritic carbonates and flysch, outcropping mostly at the eastern part of Messinia. The Pindos unit occupies mainly the eastern part of Messinia, forming a classic nappe, which has overthrusted Tripolis from east to west. The whole unit is intensively folded and faulted, forming successive thrusts of Mesozoic and early Cenozoic motion, cut by neotectonic faults of normal kinematics. The neotectonic (post-Miocene) structure of Messinia is characterized by the presence of large grabens and horsts bounded by wide fault zones, striking both N–S and E–W. The main structures are (Fig. 1) (a) the Taygetos Mt horst, (b) the Kalamata (Lower Messinia) graben, (c) the Kyparissia graben, (d) the Kyparrisia Mts. horst, (d) the Vlahopoulo graben and (e) the Pylia Mts horst. The pattern and growth of these neotectonic units are complicated because of regional uplift, crustal block rotation and normal fault development throughout the Quaternary (e.g. Armijo et al., 1992).

Historical and instrumental data show that earthquakes in Messinia are both strong and destructive. The most damaging are the shallow ones that are either the result of elastic deformation of the upper (Aegean) plate, or are caused by plate convergence along the shallow part of the Hellenic arc megathrust. The last major event in the area was the 14/2/2008 $M_w = 6.7$ earthquake, offshore southern Peloponnesus (Roumelioti et al., 2009). The most recent, onshore, disastrous earthquake was the $M_s = 6.0$ event on 13 September 1986, that occurred on a N–S striking, W-dipping normal fault, near the city of Kalamata (Lyon-Caen et al., 1988). Moreover, two moderate, onshore, shallow earthquakes, took place in 2001 near Meligalas ($M_L = 5.4$) and in 2004 near Kalamata ($M_w = 5.4$) (Figs. 1 and 2). Microseismicity investigations in the Messinia basin (Hatzfeld et al., 1990; Papoulia and Makris, 2004) have revealed the presence of several extensional NNW–SSE trending and SW dipping active features. The distribution of historical and instrumental foci and CMT solutions (1976–2010) of events with $M_w \geq 5.0$ is presented in Fig. 1. Velocity vectors after Floyd et al. (2010) displayed in the same figure, show a movement of Peloponnesus towards the SSW at a rate of about 30 mm/yr, relative to a stable Eurasia.

During the period between August and December 2011, a seismic swarm took place in the province of north Messinia, SW Peloponnesus (Chouliaras et al., 2013; Ganas et al., 2012; Fig. 1). The pattern was quite similar to the 8 May–20 September 1917 sequence, according to the "Annales de l' Observatoire National d'Athènes" and like the living memory of the local inhabitants recalled during an in situ survey

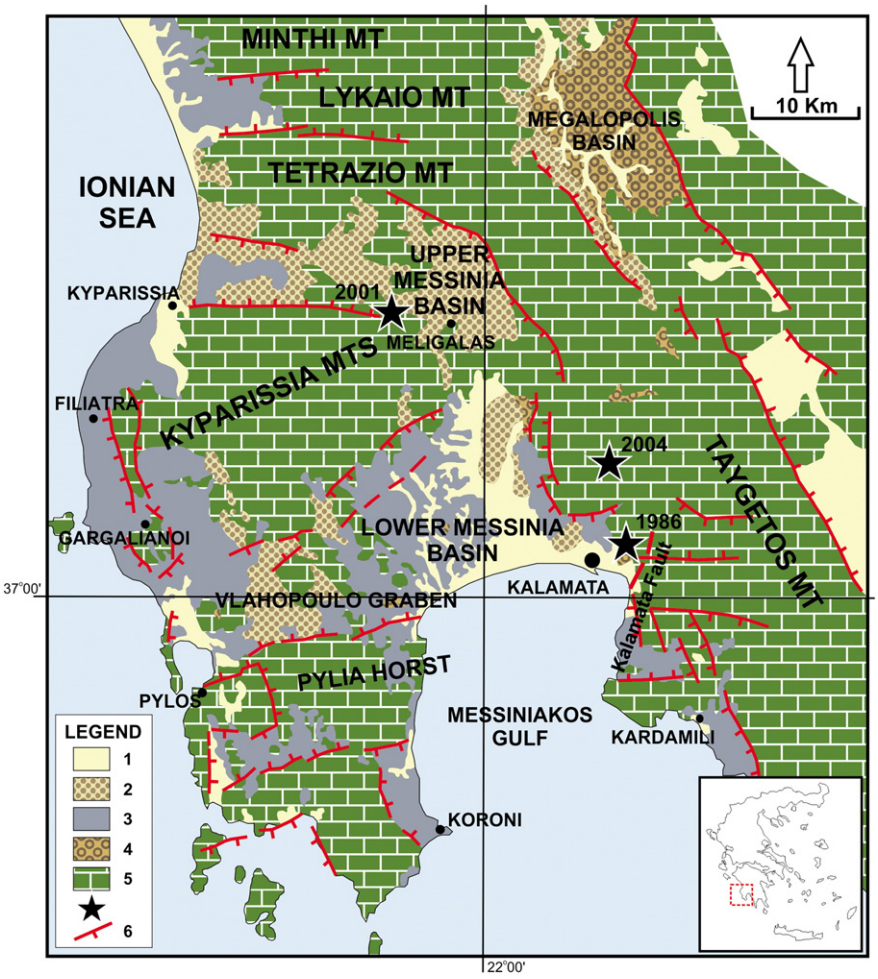

Fig. 2. Neotectonic map of SW Peloponnesus (after Ganas et al., 2012). 1: Holocene deposits, 2: Neogene–Quaternary continental deposits, 3: Neogene–Quaternary marine deposits, 4: Lacustine deposits, 5: Pre-Neogene basement (Alpine units & Messinia conglomerates), 6: Thick lines with ticks represent active fault zones. Stars: Epicenters of moderate, onshore shallow earthquakes, on 2001 near Meligalas $M_L = 5.2$ and on 2004 near Kalamata $M_L = 5.0$. The 1986 $M_s = 6.0$ shallow earthquake epicenter is also shown near Kalamata. Location of map with respect to the Hellenic arc is shown in the lower inset box.

conducted by our research group. The largest earthquakes that occurred on 14/8/2011 ($M_w = 4.8$), 14/9/2011 ($M_w = 4.6$) and 10/10/2011 ($M_w = 4.7$) were slightly damaging to a number of houses and moderately damaging to isolated cases of highly vulnerable old buildings (adobe, unreinforced with manufactured stone units). A maximum intensity VI was assessed for the event on 14/8/2011 and the cumulative maximum intensity was VI–VII following the major earthquake of 10/10/2011, according to the EMS-98 macroseismic scale (Grünthal, 1998). Those major shocks were accompanied by ground cracks in a few cases, as well as a large number of subsequent events, several of which with $M_w \geq 3.5$.

In order to acquire a high-resolution image of the 2011 swarm, we analyzed the waveform data for 1615 events by manually picking P- and S-wave arrival-times. At first, we calculated a local velocity model that minimized location errors and temporal residuals and employed it to acquire the initial solutions of hypocenters. We then applied a relocation technique in order to provide more clustered hypocenters and improve the general image of seismicity. We proceeded with spatio-temporal analysis for the investigation of possible patterns in the evolution of the seismic swarm. Focal mechanisms were calculated using regional moment tensor inversion for the strongest events and P-wave first motion polarities for a large number of smaller events, which allowed for the estimation of the geometry of the seismogenic structure. Lastly, we examined some cases of possible earthquake triggering not only due to induced local stress variations, as estimated by spatial mapping of *b*-values, but also due to Coulomb stress transferred by significant events that occurred in that area during the past decades.

2. Seismological data

The August–September part of the 2011 Oichalia swarm was recorded by the regional broadband Hellenic Unified Seismological Network (HUSN). This includes station ITM, situated about 7 km WSW of the epicentral area. In order to improve the detectability of the seismic swarm, the National and Kapodistrian University of Athens (NKUA) and the Geodynamics Institute of the National Observatory of Athens (GI-NOA) installed in common a local temporary network between 14 and 18 October 2011, complementary to HUSN. The portable network, which remained operational until the end of January 2012, was composed of three REFTEK-72A 24 bit digitizers equipped with Lennartz 3D-1 Hz sensors and four SMART-24 digitizers equipped with Lennartz 3D-20 sec sensors, with the latter transmitting data in real-time. The combined acquisition layout recorded more than 2000 events. Automatic P-wave arrival-time picking for the calculation of locations and maximum amplitude measurements used for magnitude estimations were performed in real-time, using analysis modules implemented in the acquisition system SeisComP (Heinloo and Trabant, 2004).

During a later stage, manual picking of P- and S-wave arrival-times and measurement of signal duration were performed for events recorded by at least six stations and 1615 earthquakes were successfully located using the HYPOINVERSE software (Klein, 1989), considering a

regional velocity model for the broader area of Peloponnesus (Hatzfeld et al., 1990) (Table 1). A subset of best-located events was used to extract an optimum local velocity model (Table 1) by applying the hypocentral location uncertainty minimization technique (Crosson, 1976) (Table 2). The new model yields reduced vertical (*ERZ*) and Root Mean Square (*RMS*) error values, while the mean horizontal location error (*ERH*) was slightly increased (Table 2, Fig. 3). The latter is mainly associated with a small number of events with *ERH* > 2 km (30 events with average *ERH* ≈ 6.3 km for the Hatzfeld et al. (1990) model towards 35 events with average *ERH* ≈ 9 km for the new model). However, the median *ERH* value for both models is similar (~0.73 km).

Regarding the spatial distribution, the new model provides denser clustering of the observations and a much different depth distribution (Figs. 4 and 5). The regional model tends to attract many of the shallower events of the southern part towards the surface, which is clearly an artifact, as evidenced by the large vertical location errors. The statistics for solutions of events before (47.4% of the data set) and after October 14th (52.6%), when the first temporary local stations were installed, are also presented in Table 2. As expected, the vertical location errors are greatly reduced in period #2, being constrained by the additional available local phase readings. Other than that, the median RMS remains the same (0.200 s), and the depth distribution is slightly shallower, mostly because it has also migrated to the southern portion of the activated zone. The northern cluster that was activated on 12th November 2011 (see Section 3.1) remains deeper than the rest of the events in the south, similarly to its counterpart at the beginning of the sequence.

3. Methods

3.1. Multiplet analysis/relocation procedure

The precision of the hypocentral distribution was further improved by applying the relocation algorithm HypoDD (Waldhauser and Ellsworth, 2000). This method uses the assumption that when the distance between two events' foci is much smaller than their (common) hypocentral distance from a station then their ray-paths are approximately the same and their travel-time differences can be attributed to the distance between the two foci. The algorithm operates by minimizing the double-differences between observed and calculated travel-times of P- or S-waves of neighboring events at the same station, allowing for corrections of relative hypocentral positions by reducing uncertainties caused by deviations between modeled and real velocity structure. Furthermore, cross-correlation differential travel-time data can also be incorporated into the relocation procedure, providing information on waveform similarity between strongly correlated events and taking into account their arrival-time reading consistency errors (Kapetanidis and Papadimitriou, 2011). The data between the two periods (before and after the installation of the temporary local network) intertwine because both include observed travel-times from the HUSN network (catalog links). The same is true for cross-correlation links, mostly on the closest permanent station, ITM. The relocation procedure can manage to correct the focal positions for all events using data from both periods, as there is common ground. Systematic location errors caused by either network geometry may also be decreased for the same reason.

The full waveform signals (both P- and S-wave as well as the waveform coda) of the band-pass filtered vertical component recordings of all events with available waveform data from several stations were cross-correlated to construct a combined matrix by keeping the maximum correlation value for each pair of events. The local, permanent station ITM was particularly useful for this purpose, as it is only 7 km away from the epicentral distribution, thus providing adequate cross-correlation data for the whole period of study. The temporary local stations installed between 14 and 20 October 2011, helped with the association of smaller events to the already established multiplets. Following, nearest-neighbor linkage was applied using a correlation threshold that was selected by the empirical assumption (Kapetanidis et al., 2010) that the optimal value, C_{th}, is the one which maximizes the difference between the size of the largest multiplet and the sum of clustered events (where "size" refers to the number of events contained in a multiplet). The calculated correlation threshold was $C_{th} = 0.75$ which resulted in 998 events contained in 223 multiplets (with two or more events). A sum of 406 events belongs to the 19 largest multiplets of size ≥10, with more than half of them included in multiplets of size ≥20. The location and temporal characteristics of the largest multiplets are discussed in Section 3.3.

Following, another cross-correlation procedure was applied for every combination of pairs of events in each multiplet, performed on P- or S-waves separately on each station, with initial waveform alignment on their observed arrival-times. In each case, both the cross-correlation maximum and its corresponding time-lag were registered for each of the 3 components and weighted mean values were calculated according to the waveform type analyzed in each case (P or S). The consistency between time-lag measurements and the type of component was also taken into consideration, as the P-waves are more distinctly recorded on the vertical component while the horizontal ones are more important for S-waves. This information along with the catalog travel-times, arrival-time pick weights and the custom velocity model that was used for the initial locations is then passed as input data to the HypoDD algorithm.

The parameterization of the configuration files for HypoDD was determined by trial-and-error, aimed to achieve smoothly stepped relocation with minimal event rejection and small origin shift. The HypoDD procedure was divided in 4 sets with 10 steps in total. The sets begin with low a priori weight on the cross-correlation data (CC) and high weight on catalog data (CT). Then, on the later stages, the CC weights gradually increase with decreasing CT weights. At the same time, stronger re-weighting thresholds are being applied on distance

Table 1
The 1-D velocity model from Hatzfeld et al. (1990) and the new optimal velocity model.

	Hatzfeld et al. (1990)		This study	
V_p/V_s ratio	1.773		1.770	
Layer	P-wave velocity (km/s)	Ceiling depth (km)	P-wave velocity (km/s)	Ceiling depth (km)
1	5.8	0.0	4.5	0.0
2	6.0	10.0	5.1	4.0
3	6.4	20.0	6.1	10.0
4	8.0	40.0	6.5	21.0
5	–	–	7.1	31.0
6	–	–	7.6	46.0
7	–	–	7.9	60.0
8	–	–	8.2	75.0

Table 2
Statistics of location/RMS errors and depth distribution comparing the two models. Period #1 consists of events that occurred before the installation of the first temporary local stations (October 14th 2011), while period #2 consists of the events that occurred after October 14th.

Model	Hatzfeld et al. (1990)	This study (all events)	This study (period #1)	This study (period #2)
Mean RMS	0.227	0.224	0.242	0.207
Median RMS	0.200	0.200	0.200	0.200
Mean ERH	0.867	0.947	1.049	0.855
Mean ERH < 2 km	0.763	0.763	–	–
Median ERH	0.729	0.727	0.700	0.744
Median ERH < 2 km	0.725	0.721	–	–
#evt with ERH > 2 km	30	35	–	–
Mean ERZ	2.588	1.160	1.639	0.731
Median ERZ	1.240	0.560	0.700	0.440
Mean depth	7.050	8.670	8.874	8.481
Median depth	7.080	8.820	8.950	8.680

between linked event-pairs and residuals on both types of data. This achieves a crude relocation of the whole distribution in the first sets and refined relocation concentrated on multiplets at the later sets.

Starting with 1516 sufficiently linked events, 1480 were successfully relocated, representing 91.6% of the full catalog. The mean origin shift was ~22 m, which is important, as it shows that there is only minimal systematic shift of the hypocenters and that the events' locations were mostly concentrated closer to the main body of the original distribution or to their cluster's centroid. This result is displayed in Figs. 6B and 7B in comparison to the initial locations (Figs. 6A and 7A).

The 3D distribution of the relocated events has been divided into 6 spatial clusters (labeled as shown in Figs. 6B and 7B) using ward linkage, which works better with Euclidean distances. This discrimination makes it easier to understand how the events in each group were relocated, but will also be helpful during the description of the spatio-temporal distribution that is discussed in Section 3.3. The number of events in each cluster is 179, 205, 149, 584, 190 and 173 for clusters #1 to #6 respectively. Concentrations within individual clusters during the relocation procedure are mainly due to strongly correlated events that form multiplets. A least-squares best-fit plane has been calculated from the 3D distribution of the relocated hypocenters, striking N177°E with a dip angle ~W18°. The cross-sections of Fig. 7, which are almost parallel to the strike of the aforementioned plane, also indicate that the seismicity tends to be deeper in the North than in the South, although this does not imply that the fault is dipping NNW. The total length of the spatial distribution is ~18 km in the NNW–SSE direction.

Furthermore, the major $M_w = 4.8$ event of 14 August 2011 which started the sequence, is located at a gap in the spatial distribution between clusters #1 and #2 in the northern tip and has been classified to the latter one. The gap around the major event is consistent with the rupture of an asperity that caused redistribution of stress in its neighboring region, triggering clusters #1 and #2. Other identifiable gaps are separating clusters #2 and #4 from the slightly shallower #3 and #5 respectively, but these can't be directly associated with a major shock. Some smaller sub-clusters belonging to #4 also seem to be more detached from the main body of the cluster. However, following the current clustering hierarchy, a threshold constructing at least 10 spatial clusters would be required for their partition, which was not deemed necessary for the description of the seismic swarm activity.

Fig. 8 shows cross-sections of the relocated hypocenters at azimuth N75°E, almost perpendicular to the main direction of the swarm's distribution, at three partially overlapping segments. The low dip angle

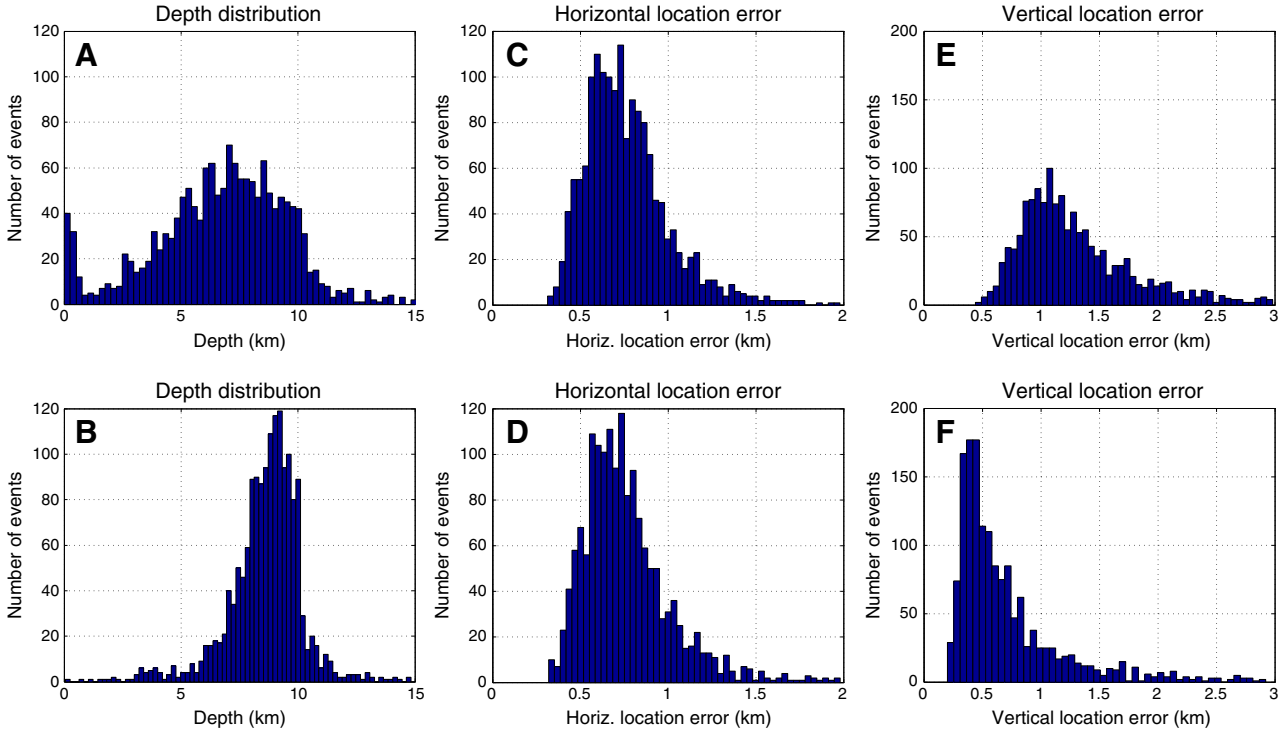

Fig. 3. Distribution A) of depths with the velocity model of Hatzfeld et al. (1990), B) with the new model calculated in this paper, C) of horizontal location errors with the velocity model of Hatzfeld et al. (1990), D) with the new model calculated in this paper, E) of vertical location errors with the model of Hatzfeld et al. (1990) and F) with the new model calculated in this paper.

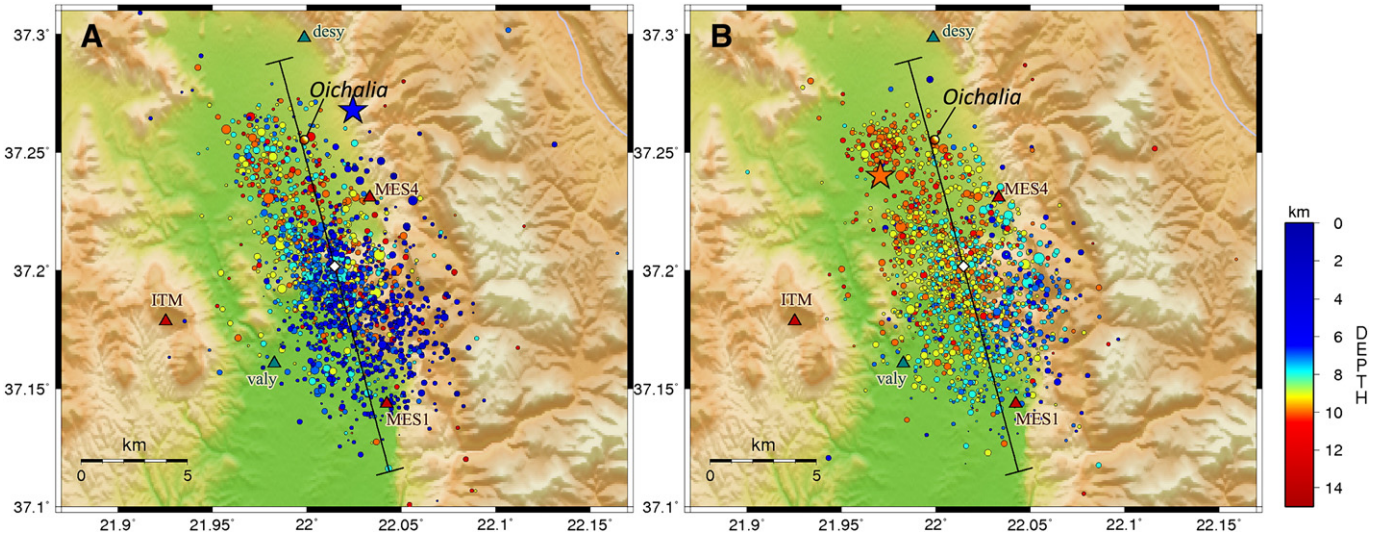

Fig. 4. Epicenters of 1615 located earthquakes A) with the regional velocity model by Hatzfeld et al. (1990) and B) with the new local model calculated in this paper. The common color-scale represents variability in depth, with the gradient between 6 and 11 km corresponding to the approximate range of depths calculated using the new velocity model. The line drawn at N165°E azimuth, centered at 37.2018°N, 22.0148°E (white diamond) is used for the cross-sections of Fig. 5. The star denotes the major event of 14 August 2011. Local stations are represented by triangles.

of the fault is more prominent in its deeper portion, as seen at the northernmost segment (b_1–b_2). In the middle cross-section (c_1–c_2) the shallower cluster #5 tends to connect to the rest of the distribution at a higher angle, almost 45°. It is evident from the comparison between the parallel (Fig. 7) and perpendicular cross-sections (Fig. 8) that the distribution is becoming shallower primarily towards ENE rather than SSE, which is consistent with a low-angle fault striking SSE–NNW and dipping WSW.

Concerning the accuracy and location errors of the relocated hypocenters, the covariance matrix of the conjugate gradients method (LSQR), which is used for large systems such as the Oichalia earthquake swarm that is being studied in this work, tends to grossly underestimate errors (Waldhauser, 2001). For this reason, it is important that error assessment is done by applying statistical resampling methods such as jackknife and bootstrap (Efron, 1982; Efron and Tibshirani, 1993), following the approach suggested by Waldhauser and Ellsworth (2000).

In order to examine the influence of the stations' distribution to the relocation results we performed a jackknife test, repeating the relocation procedure after removing one station at a time. Only the 7 stations of the local network were considered, along with station ITM of the HUSN network (8 repetitions of relocation in total), as these are the closest and most important ones. For each relocation on the resampled data the difference in the relocated hypocenter of every event was measured relative to its corresponding locus derived from the relocation performed with all stations.

Ellipsoids are calculated for both the epicentral and 3D distributions, bounding the 95% confidence interval for all observations (all events for all resampled relocation results). The length of the projection of the ellipsoids' semi-axes as well as the mean, median and standard deviation values of the difference in horizontal (*dx* for E–W and *dy* for N–S orientation) and vertical (*dz*) positions are registered in Table 3 for the whole period of study and, also, for each of the two periods (before and after the installation of the local network) separately.

The influence of station ITM was also examined. Statistics labeled "no ITM" in Table 3 were calculated for observations of events which were successfully relocated in all 8 repetitions of the relocation procedure, as described above (each repetition includes the elimination of one of the 7 local stations or station ITM), thus these errors include the case where ITM has been removed. Statistics labeled "with ITM" have been calculated for only 7 repetitions of relocation, with elimination of the 7 local stations, one at a time, but always retaining the data

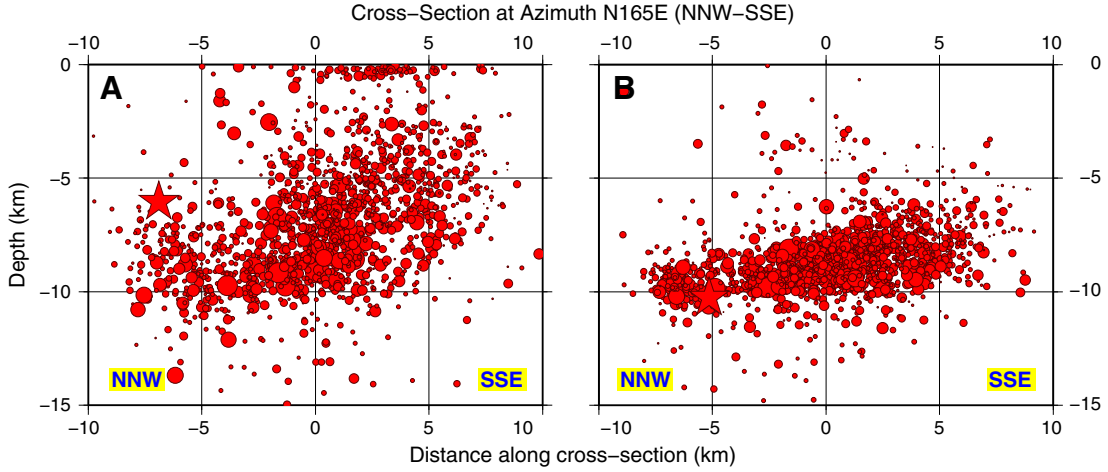

Fig. 5. Cross-section of the 1615 located earthquakes at N165°E direction (NNW–SSE), centered at 37.2018°N, 22.0148°E (see Fig. 4), (A) with the regional velocity model (Hatzfeld et al., 1990) and (B) with the new local model calculated in this paper. The star denotes the major event of 14 August 2011.

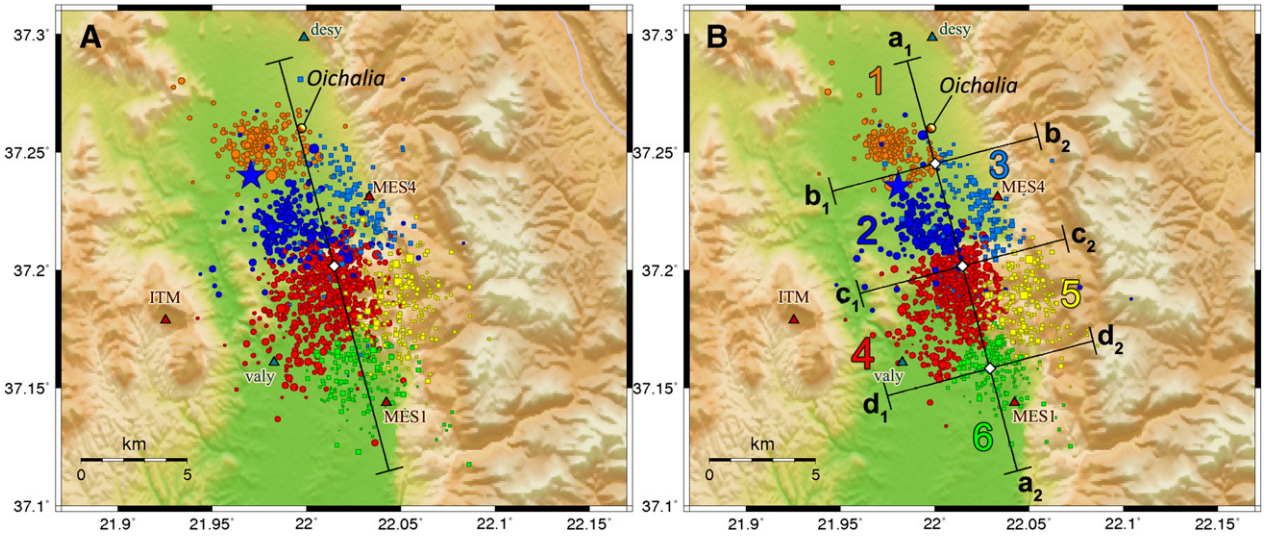

Fig. 6. Epicenters of the seismic swarm sequence A) before and B) after relocation with HypoDD. Colors and numbers (Panel B only) correspond to 6 major spatial clusters that could be distinguished. The profile line a_1–a_2, drawn at N165°E azimuth, is used for the cross-sections of Fig. 7, while the lines b_1–b_2, c_1–c_2 and d_1–d_2, drawn at N75°E azimuth, perpendicular to the main axis of the swarm's distribution, are used for the cross-sections of Fig. 8. The star denotes the major event of 14 August 2011. Local stations are represented by triangles.

from station ITM, which is crucial especially for the first period (before the installation of the local network).

The mean relative location error values range roughly between 35 and 150 m for the horizontal offsets and 50 m–185 m for the vertical offset, while the median values, which, contrary to the mean ones are not influenced by outliers, are much smaller, of the order of a few tens of meters. Standard deviations are of the order of a few hundreds of meters, in most cases, while the 95% confidence interval (c.i.) is about 2.4 times larger than the standard deviation. Events of period #1 (before 14 October 2013) seem to be less influenced by the station geometry, especially in the "with ITM" case, which purely shows the influence of the temporary local stations. This is expected, as the data of period #1 are only indirectly linked with the local stations (with events of period #2) through links available from station ITM and other regional stations. In general, events of period #2 seem to be more affected by the local station geometry. Station ITM plays an important role, for both the horizontal and vertical distributions, especially for period #1 (i.e. 95% c.i. for *dz* reaches about 2 km for the "no ITM" case) and for the linkage between events of the two periods. There is a small bias favoring an E–W orientation, which, being almost perpendicular to the main direction of the swarm's spatial distribution, does not affect the general results.

A similar jackknife technique was used to measure the influence of each event. Multiple relocation procedures were applied by removing one event at a time and measuring the location differences (Waldhauser and Ellsworth, 2000; Waldhauser and Richards, 2004). The events' influence, as expected for the relatively large system of ~1500 events of this study, is small. The absolute mean values are of the order of a few meters, with standard deviation of a few tens of meters and 95% c.i. reaching a maximum of 260 m for the vertical axis in period #1. The *dx* and *dy* values are almost similar, indicating no bias in any particular horizontal direction. They are also similar in both periods, while *dz* values are larger for period #1, apparently affected by the absence of direct data from local stations. The small

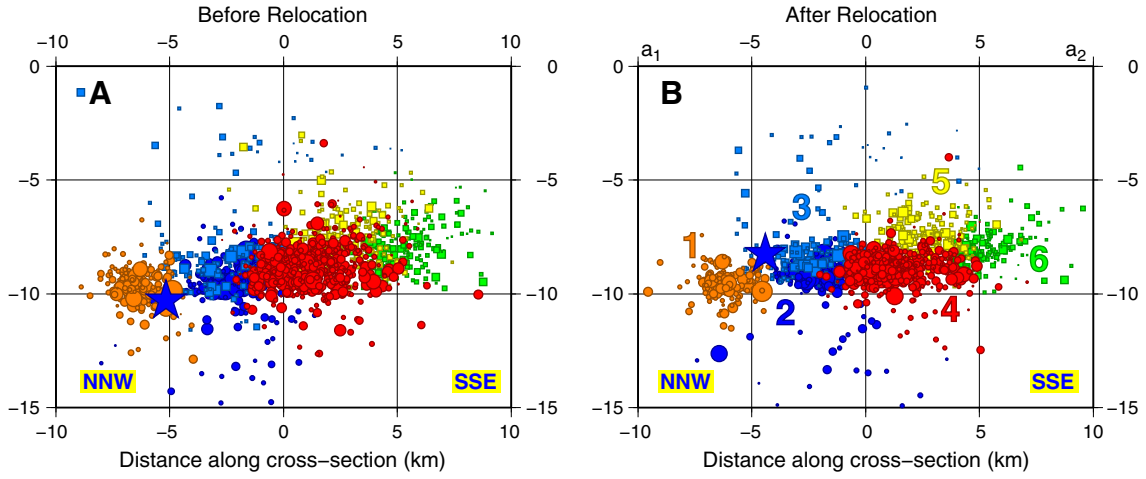

Fig. 7. Cross-section of the seismic swarm sequence at N165°E direction (NNW–SSE), parallel to the main direction of the seismicity distribution, centered at 37.2018°N, 22.0148°E (central white diamond in Fig. 6), A) before and B) after relocation with HypoDD. Colors and numbers represent the 6 spatial clusters that were discriminated and correspond to the same color/number labels as shown in Fig. 6B. The star denotes the major event of 14 August 2011.

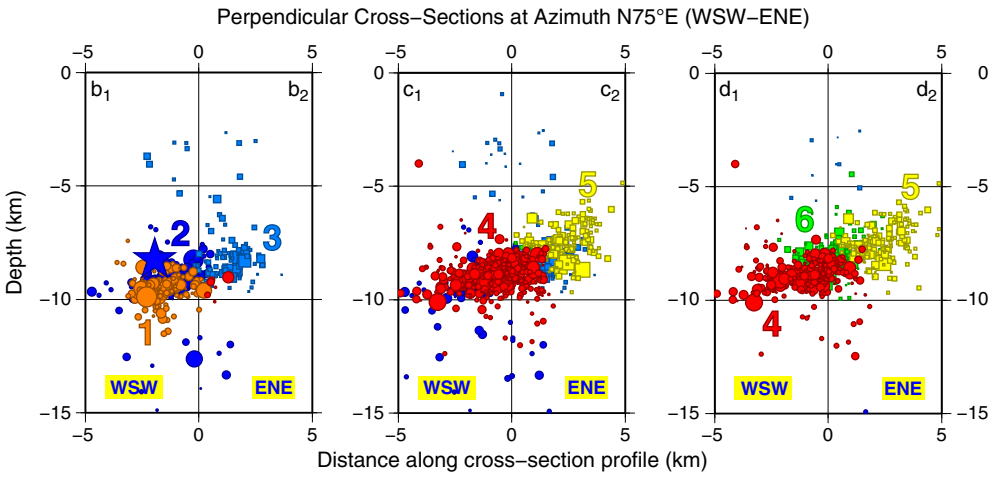

Fig. 8. Cross-section of the relocated hypocenters of the swarm sequence at N75°E direction (NNW–SSE), perpendicular to the main direction of the seismicity distribution, along profile lines shown in Fig. 6B: (b_1–b_2) Northern segment, centered at 37.2452°N, 22.0002°E (northern white diamond in Fig. 6B), (c_1–c_2) middle segment, centered at 37.2018°N, 22.0148°E (middle white diamond in Fig. 6B), (d_1–d_2) Southern segment, centered at 37.1584°N, 22.0294°E (southern white diamond in Fig. 6B). Colors and numbers represent the 6 spatial clusters that were discriminated and correspond to the same color/number labels as shown in Fig. 6. The width of each of the cross-sections is ±4 km, with about 2 km overlap. The star denotes the major event of 14 August 2011.

relative errors measured in this test indicate that each event is well linked with many of its neighbors, thus it is not affected by the elimination of a single neighbor (Wilcock, 2012).

The influence of the initial hypocentral locations (starting model) to the results was estimated with a bootstrap method, by performing multiple relocation procedures after perturbing the initial locations by a small random amount, within the limits of the absolute location error. Random numbers are selected from a normal distribution, generated between roughly −1 and +1, multiplied by the estimated location error (*ERX*, *ERY*, *ERZ*) on each of the 3 axes for each event separately and added to its catalog location. This procedure was repeated 300 times and the corresponding statistical values were calculated for the whole

Table 3
Relative error estimates for the relocation results using statistical resampling. "Per." stands for "period", P1 and P2 are for before and after 14 October 2013, respectively. The offset *dx*, *dy* and *dz* (for projections in the E–W, N–S and Z axis, respectively) are the difference of the relocated positions for the resampled data in comparison to the original relocation results. More details in the text.

Test	Per.	Offset (m)	Abs. mean (m)	abs. median (m)	St. dev. (m)	95% c.i. (m)
Stations (no ITM)	ALL	*dx*	110	35	260	640
		dy	110	35	250	610
		dz	185	45	580	1420
	P1	*dx*	50	20	100	245
		dy	50	20	110	270
		dz	80	30	770	2160
	P2	*dx*	150	60	330	815
		dy	150	60	315	770
		dz	170	60	370	1050
Stations (with ITM)	ALL	*dx*	85	30	230	565
		dy	85	30	215	525
		dz	100	35	250	705
	P1	*dx*	35	15	65	165
		dy	35	15	65	160
		dz	50	25	150	415
	P2	*dx*	130	50	310	760
		dy	130	50	285	700
		dz	145	55	315	895
Events	ALL	*dx*	3	0.9	13	35
		dy	3	0.8	13	35
		dz	6	1.0	65	185
	P1	*dx*	3	0.9	10	30
		dy	3	0.9	15	40
		dz	7	1.0	90	260
	P2	*dx*	3	0.8	15	35
		dy	3	0.8	15	35
		dz	6	1.0	25	75
Robustness	ALL	*dx*	35	20	85	215
		dy	35	20	70	165
		dz	90	45	200	565
	P1	*dx*	30	20	55	140
		dy	30	20	60	145
		dz	90	40	225	630
	P2	*dx*	40	25	105	260
		dy	35	25	75	185
		dz	90	50	175	505

Table 4
Catalog of Moment Tensor solutions for the 18 largest earthquakes of the swarm. The hypocentral locations are HypoDD solutions. Asterisks in the rank column denote NOA MT solutions.

Rank	Origin time	Lon (°)	Lat (°)	MT depth (km)	HypoDD depth (km)	M_w	Strike (°)	Dip (°)	Rake (°)	Misfit	CLVD (%)
1	2011 08 14 01:05	21.9806	37.2356	13	8.25	4.8	150	39	−75	A	23.8
2	2011 08 16 01:14	21.9773	37.2520	5	9.48	3.6	153	31	−91	C	10.8
3	2011 08 19 16:33	21.9988	37.2152	7	9.32	3.7	140	20	−80	C	8.4
4*	2011 08 22 08:50	21.9896	37.2284	10	7.47	4.1	168	41	−83	B	32.1
5	2011 08 23 05:22	21.9850	37.2200	7	9.37	4.0	182	48	−62	B	3.0
6	2011 09 14 03:35	22.0314	37.1680	10	8.81	4.6	184	40	−44	B	22.3
7	2011 09 15 07:54	22.0140	37.2043	10	8.67	3.7	170	45	−95	C	1.5
8	2011 09 15 08:16	22.0068	37.2173	8	8.25	3.9	180	40	−35	C	12.2
9	2011 10 07 04:29	22.0627	37.2158	12	8.25	3.9	190	65	−80	B	6.8
10	2011 10 07 11:32	22.0400	37.2021	12	8.60	3.8	230	15	−100	C	18.8
11*	2011 10 10 01:20	22.0474	37.1894	9	8.36	4.3	174	50	−62	B	20.7
12*	2011 10 10 04:49	22.0502	37.2046	11	8.69	4.3	190	30	−50	B	7.9
13	2011 10 10 19:07	22.0417	37.1883	11	11.1	4.7	195	31	−90	C	3.9
14	2011 10 10 19:15	22.0494	37.1937	9	6.19	3.8	169	31	−96	B	15.2
15	2011 10 10 21:17	22.0290	37.2129	15	8.25	3.9	180	55	−45	C	14.8
16*	2011 10 11 01:10	22.0132	37.1955	4	8.53	4.0	176	32	−62	C	14.8
17	2011 10 15 22:06	22.0715	37.1732	5	5.00	3.9	158	22	−87	B	16.3
18	2011 11 12 18:28	21.9804	37.2303	4	9.88	4.1	177	37	−56	B	17.5

set of observations. As shown in Table 3, the test of robustness against variation of initial conditions (starting model) resulted in mean horizontal and vertical relative location errors of less than 40 m and 95 m, respectively. The 95% confidence intervals show that the majority of observations lie within ~200 m horizontally and ~550 m vertically, again with a small bias towards the E–W direction.

3.2. Fault plane solutions

Moment tensor solutions have been calculated for 14 events using local and regional data. Additionally, 128 focal mechanisms of smaller events were determined by first motion polarities. Four fault plane solutions registered in the NOA MT catalog were also considered.

Broadband waveform data from the Hellenic Unified Seismological Network (HUSN) were collected and analyzed in order to determine the source parameters of the largest events of the Oichalia swarm. The source parameters of 14 earthquakes with magnitudes $M_w \geq 3.6$ were calculated based on moment tensor inversion using regional waveforms (epicentral distances less than 3°). Typically, the use of at least four stations well distributed azimuthally and within an epicentral radius, less than 200 km, is quite capable for this purpose. The data preparation includes bandpass filtering between 0.05 Hz and 0.7 Hz, deconvolution of the instrumental response, integration to displacement and rotation of the horizontal components towards the back azimuth. Following, the signal was inverted using the reflectivity method of Kennett (1983) as implemented by Randall (1994) in order to determine Green's Functions. Initially, iterative inversions were performed, considering a crude depth interval of 5 km and the relative misfit functions were computed. In a second stage, inversions were performed at a finer interval of 1–2 km around the depth where the lowest misfit was exhibited. During the analysis, various 1D velocity models were used, depending on the geographic location of stations (i.e. Drakatos et al., 2002; Haslinger et al., 1999; Karagianni et al., 2005; Novotny et al., 2001; Papazachos and Nolet, 1997).

The quality of the results of moment tensor solutions was evaluated by considering the average misfit and the percentage of Compensated Linear Vector Dipole (CLVD). For each of the determined focal mechanisms, a quality code represented by letters A–D (best–worst) was adapted for the minimum misfit. The MT inversion solutions are listed in Table 4. The hypocentral parameters adopted for the MT fault plane solutions are those obtained from the relocation procedure, as described in the previous section.

The local network geometry and station spacing allowed the determination of fault plane solutions using P-wave first-motion polarities. Concerning the recordings of the local network, P-wave onset directions were manually observed and registered. First-motion polarity observations available from the HUSN were also incorporated. Following, equal area projections of the lower hemisphere were constructed. Focal mechanism solutions were constrained by at least six P-wave first motions. Take-off angles were computed based on the new seismic velocity model (Table 1). The quality of the polarity readings and the azimuthal coverage on the focal sphere were also taken into consideration. The first-motion patterns can be adequately modeled by pure double-couple (DC) sources, although the data points are not dense enough to exclude the presence of a significant non-DC source component. The quality of the focal mechanism solutions varies considerably from moderately to well constrained, depending on the data coverage of the focal sphere. Among numerous solutions that were determined, a total of 128 were adopted, with ~10° uncertainty for the nodal planes (Table 5).

The results are illustrated in Fig. 9. As it can be observed, the majority of focal mechanisms exhibit normal faulting in almost N–S direction, compatible with superficial fault traces (Armijo et al., 1992) and inferred from seismicity (Lyon-Caen et al., 1988) and GPS data (Nyst and Thatcher, 2004). As expected, the larger magnitude MT solutions ($M_w \geq 3.6$), which represent a larger scale of deformation across the fault surface, exhibit relatively homogeneous distribution of the nodal planes, striking N ~ 175° and dipping W ~ 37° at an average depth of 8.5 km. The smaller magnitude P-wave first motion polarity solutions, despite their implication for a quite similar dip-slip normal faulting in a N ~ 163° direction with an average W ~ 47° dip, present significant heterogeneity towards the south, where several strike-slip and a few reverse focal mechanisms are also observed. Cross-sections performed perpendicular and parallel to the activated structure (Fig. 10) imply for a low angle normal dip-slip fault plane, striking roughly N160°E and dipping WSW32°. This is partly incompatible with the ~18° WSW dipping of the hypocenter distribution (Figs. 8 and 10), but may correspond to a rupture towards a shallower section of the fault, e.g. a continuation of the segment corresponding to the spatial cluster #5 towards NNW, which is distributed at a higher dip angle (Fig. 8, cross-section c_1–c_2). The implied geometry of the activated fault zone, is also consistent with the CMT fault planes of the co-located $M_w = 5.4$, 16/9/2001 and the $M_w = 5.4$, 3/1/2004 events (striking N130° and N211°, respectively), which are listed in Table 6. It is probable that more than one structures are involved, interacting with each other, forming a complex fault network which is compatible with the tectonic graben of Oichalia. Intraplate swarms are generally explained as the consequence of a very heterogeneous stress field and a weakened crust that lacks a single well-developed fault and is incapable of sustaining higher strain (Horálek and Fischer, 2008). This pattern is consistent with the one

Table 5
Catalog of P-wave first motion polarity solutions. The hypocentral locations are HypoDD solutions.

Rank	Origin Time	Lat. (°)	Lon. (°)	Depth (km)	M_L	Strike (°)	Dip (°)	Rake (°)
1	2011 10 23 11:58	37.2329	22.0045	3.5	2.0	200	74	−60
2	2011 10 23 22:23	37.1918	21.9799	7.9	1.8	154	50	−2
3	2011 10 23 22:54	37.1760	22.0132	6.4	1.3	289	60	−125
4	2011 10 23 22:57	37.1754	22.0166	6.5	1.8	289	70	−110
5	2011 10 24 01:19	37.2005	22.0107	5.9	1.5	159	50	−90
6	2011 10 24 02:48	37.1862	21.9934	6.5	1.6	159	50	−2
7	2011 10 24 05:48	37.1761	22.0701	9.2	2.5	224	35	−35
8	2011 10 24 21:59	37.1872	22.0329	9.0	1.4	35	70	−35
9	2011 10 25 00:14	37.1576	22.0269	3.8	1.5	5	20	−90
10	2011 10 25 01:16	37.1774	22.0316	3.7	1.9	140	35	−80
11	2011 10 25 02:48	37.1632	22.0387	3.7	2.1	164	45	−50
12	2011 10 25 10:11	37.2335	22.0283	1.6	2.4	144	45	−75
13	2011 10 25 18:12	37.1943	21.9960	6.9	2.3	154	45	−70
14	2011 10 25 19:26	37.1859	22.0647	4.4	1.8	82	79	−160
15	2011 10 25 21:36	37.2052	22.0108	4.4	2.0	169	60	−110
16	2011 10 26 10:07	37.1655	22.0395	3.8	1.8	159	25	−70
17	2011 10 26 12:13	37.1605	22.0040	8.1	2.4	174	67	−110
18	2011 10 26 19:11	37.2169	22.0334	1.6	3.3	159	86	−70
19	2011 10 26 22:02	37.1774	22.0471	0.2	1.7	200	45	−100
20	2011 10 26 22:23	37.1605	22.0140	2.0	2.6	159	45	−90
21	2011 10 27 01:19	37.1547	22.0013	7.2	2.2	144	45	−110
22	2011 10 27 01:31	37.1845	22.0272	4.4	1.5	95	79	−70
23	2011 10 27 02:40	37.1877	22.0124	3.4	1.7	174	60	−50
24	2011 10 27 04:52	37.2190	22.0409	1.4	2.5	235	30	−150
25	2011 10 28 00:06	37.1672	22.0288	6.8	2.2	4	19	−90
26	2011 10 28 00:09	37.1705	22.0512	3.5	1.9	144	30	−70
27	2011 10 28 07:03	37.1609	22.0004	7.6	2.6	164	54	−110
28	2011 10 28 08:11	37.1595	22.0043	7.2	3.0	275	15	−90
29	2011 10 28 08:41	37.1611	22.0176	6.1	2.3	154	60	−110
30	2011 10 28 09:46	37.1595	22.0065	6.1	2.6	157	45	−110
31	2011 10 28 10:13	37.1633	21.9991	8.5	2.6	157	50	−110
32	2011 10 28 22:06	37.1991	22.0196	3.3	1.9	144	60	−65
33	2011 10 29 06:33	37.1960	22.0058	4.8	1.8	144	50	−65
34	2011 10 29 14:36	37.1742	22.0201	6.0	2.1	157	59	−110
35	2011 10 29 17:43	37.2021	22.0132	3.5	1.9	149	62	−110
36	2011 10 29 19:51	37.1642	22.0083	6.3	2.4	30	45	−125
37	2011 10 30 01:35	37.1701	22.0358	3.5	1.5	159	39	125
38	2011 10 30 01:51	37.1724	22.0164	4.1	2.3	30	50	−120
39	2011 10 30 02:25	37.1957	22.0114	5.7	0.4	140	45	−65
40	2011 10 30 04:10	37.2370	21.9711	14.8	1.4	140	45	−65
41	2011 10 30 08:14	37.1593	22.0668	0.9	2.4	159	70	−60
42	2011 10 30 10:33	37.1541	22.0362	3.2	2.0	159	30	−35
43	2011 10 30 10:51	37.2133	21.9849	7.4	1.9	214	54	−35
44	2011 10 30 14:55	37.1635	22.0285	6.4	1.8	214	50	−90
45	2011 10 30 19:40	37.1693	22.0189	7.5	2.3	190	19	−90
46	2011 10 30 20:09	37.1756	22.0355	4.7	1.6	169	67	−50
47	2011 10 31 12:58	37.1734	22.0484	0.9	1.7	159	45	−110
48	2011 10 31 16:32	37.2023	22.0148	4.7	0.9	164	65	−35
49	2011 10 31 18:07	37.1758	22.0340	5.5	1.5	115	35	−90
50	2011 10 31 21:06	37.2114	22.0090	5.8	1.3	115	54	−90
51	2011 10 31 21:33	37.2104	22.0118	2.2	1.1	109	60	−90
52	2011 10 31 22:18	37.1821	22.0430	3.8	1.5	159	84	−90
53	2011 10 31 23:08	37.1956	22.0176	6.2	1.5	115	54	−90
54	2011 10 31 23:24	37.2003	22.0399	3.0	1.7	159	50	−65
55	2011 10 31 23:35	37.1627	22.0185	4.0	1.0	140	39	−120
56	2011 11 01 00:42	37.2056	22.0128	3.8	0.6	169	50	−60
57	2011 11 01 02:28	37.2022	22.0111	2.2	0.8	169	65	−60
58	2011 11 01 06:43	37.1967	22.0219	3.1	1.0	169	65	−60
59	2011 11 01 11:31	37.1664	22.0019	3.9	1.7	180	54	−55
60	2011 11 01 13:08	37.1696	22.0105	4.6	1.4	309	86	−90
61	2011 11 01 13:26	37.1944	22.0213	7.8	1.4	169	65	−60
62	2011 11 01 17:42	37.1906	22.0328	3.9	1.2	169	45	−70
63	2011 11 01 19:52	37.1820	21.9938	4.6	1.3	169	45	−60
64	2011 11 01 23:01	37.1710	22.0271	3.0	1.2	109	35	−90
65	2011 11 01 23:29	37.1621	22.0054	7.0	1.2	79	79	−90
66	2011 11 02 00:26	37.1803	21.9857	5.4	1.2	70	54	−55
67	2011 11 02 02:21	37.1635	21.9962	5.4	0.8	159	9	−90
68	2011 11 02 03:00	37.1689	22.0709	1.5	0.7	159	65	−55
69	2011 11 02 04:12	37.2034	22.0190	3.7	0.9	159	65	−55
70	2011 11 02 07:12	37.1871	22.0012	4.8	1.9	169	67	−50
71	2011 11 02 09:42	37.1579	22.0100	6.0	1.4	154	35	−70
72	2011 11 02 10:42	37.2035	22.0207	2.0	1.1	144	54	−75
73	2011 11 02 17:43	37.1597	21.9962	2.8	1.2	142	26	−65
74	2011 11 02 19:53	37.1537	22.0025	6.2	2.4	289	82	100
75	2011 11 02 20:06	37.1598	21.9966	1.4	1.2	289	72	100
76	2011 11 02 20:33	37.1598	21.9941	5.0	1.8	293	72	−90

(continued on next page)

Table 5 (*continued*)

Rank	Origin Time	Lat. (°)	Lon. (°)	Depth (km)	M_L	Strike (°)	Dip (°)	Rake (°)
77	2011 11 02 20:49	37.2358	22.0235	3.6	1.9	293	72	−90
78	2011 11 03 00:32	37.1799	21.9903	5.6	1.6	293	65	−90
79	2011 11 03 00:40	37.1807	21.9998	5.9	1.8	293	65	90
80	2011 11 03 02:28	37.1814	21.9911	5.6	1.0	293	65	−90
81	2011 11 03 03:41	37.1856	21.9893	5.9	0.8	293	54	−90
82	2011 11 03 04:33	37.1670	22.0323	3.3	1.6	293	65	−90
83	2011 11 03 05:17	37.2054	22.0139	4.1	1.7	169	65	−100
84	2011 11 03 06:42	37.1628	22.0455	3.2	2.3	169	74	−65
85	2011 11 03 17:24	37.1778	22.0277	3.7	1.0	149	50	−85
86	2011 11 03 17:35	37.1648	22.0458	3.8	1.0	159	47	−60
87	2011 11 03 23:30	37.1952	21.9872	5.3	1.4	159	47	−90
88	2011 11 04 05:28	37.2178	22.0372	7.5	1.5	159	79	−100
89	2011 11 04 06:00	37.1567	22.0335	7.7	1.4	289	79	−90
90	2011 11 04 14:18	37.1631	22.0008	5.7	2.0	109	86	−80
91	2011 11 04 16:00	37.1639	21.9881	8.3	2.0	154	30	−140
92	2011 11 04 16:09	37.1565	22.0425	0.1	1.1	289	79	−95
93	2011 11 04 21:40	37.1626	21.9924	3.8	1.5	174	39	−65
94	2011 11 05 06:13	37.1642	22.0316	4.9	1.2	164	25	−70
95	2011 11 05 08:25	37.1847	22.0157	5.3	1.1	289	45	90
96	2011 11 05 08:44	37.2047	22.0110	1.1	1.0	159	25	−70
97	2011 11 05 11:18	37.2135	22.0051	5.7	1.1	180	56	−70
98	2011 11 05 15:24	37.2115	22.0220	6.7	1.1	185	60	−80
99	2011 11 05 17:00	37.2134	22.0404	2.6	1.0	109	62	−90
100	2011 11 05 19:43	37.1944	22.0092	5.3	1.2	159	53	−50
101	2011 11 06 05:26	37.1701	22.0319	3.9	0.9	174	70	−30
102	2011 11 06 10:01	37.2341	22.0090	3.5	1.5	169	65	−30
103	2011 11 06 10:17	37.2270	22.0371	1.8	1.6	169	65	−65
104	2011 11 06 20:34	37.2118	22.0112	4.3	1.3	169	65	−65
105	2011 11 08 02:33	37.1791	22.0463	3.3	1.9	174	39	−60
106	2011 11 08 05:07	37.1519	22.0222	5.8	1.0	130	30	−100
107	2011 11 08 06:22	37.2125	22.0458	2.1	1.1	130	65	−85
108	2011 11 08 10:32	37.1601	22.0336	6.5	1.2	240	72	−50
109	2011 11 08 20:25	37.1630	22.0166	6.7	1.6	230	72	60
110	2011 11 08 23:41	37.1654	22.0295	5.4	0.9	109	30	90
111	2011 11 09 02:24	37.1836	22.0433	3.3	1.1	109	30	−90
112	2011 11 09 03:57	37.1815	22.0249	3.6	2.0	125	45	−125
113	2011 11 09 04:05	37.1636	22.0333	2.4	1.6	185	65	130
114	2011 11 09 15:21	37.2070	22.0101	4.0	1.2	174	54	−50
115	2011 11 09 17:25	37.1828	21.9990	3.9	0.5	174	54	−50
116	2011 11 09 18:22	37.1991	21.9859	6.3	0.8	174	54	−40
117	2011 11 09 19:15	37.1695	22.0288	4.5	1.0	174	50	−40
118	2011 11 09 22:20	37.1811	22.0043	4.4	1.7	289	57	140
119	2011 11 09 22:20	37.1811	22.0043	6.6	2.2	289	57	140
120	2011 11 10 06:15	37.1784	21.9986	3.0	0.7	174	50	−40
121	2011 11 10 09:23	37.1513	22.0255	4.0	1.3	0	74	−145
122	2011 12 01 00:19	37.2556	21.9676	9.3	1.3	169	60	−65
123	2011 12 01 01:19	37.253	21.9742	9.2	2.3	169	60	−65
124	2011 12 01 01:56	37.2529	21.9682	9.3	1.3	169	60	−65
125	2011 12 01 02:29	37.2466	21.954	2.5	1.3	169	60	−65
126	2011 12 01 02:41	37.2569	21.9737	6.7	0.9	169	70	−65
127	2011 12 01 03:16	37.1905	22.0212	0.3	1.2	169	50	−65
128	2011 12 01 03:52	37.2614	21.9707	7.6	1.3	169	50	−65

observed in the rapidly opening western Corinth graben, where seismic strain is hosted on E–W low angle normal faults (Bernard et al., 1997; Rigo et al., 1996), cross-cutting older structures which have been known to generate swarms under the influence of fluids (Lyon-Caen et al., 2004; Pacchiani and Lyon-Caen, 2010).

The relatively inhomogeneous types of the smaller events focal mechanisms that is evident at the southern part of the swarm is unlikely an artifact, as the nodal planes solutions adopted represent robust determinations, undergone strict qualification criteria. On the other hand, it is typical for events in earthquake swarms to be characterized by a combination of strike-slip and normal faulting mechanisms (e.g. Hill, 1977; Lay and Wallace, 1995). A possible explanation (Rigo, 2010) is that the diffuse activity might probably be enhanced by fluid interaction with the activated fault plane, as the presence of fluids may impose an increased non-double-couple component (volumetric, CLVD) to the moment tensors. It is worth mentioning that a large CLVD component was defined during the 14-8-2011 major event ($M_w = 4.8$), of the order of 32.1%, increasing suspicions for the fluid hypothesis.

Fig. 11 presents the geometry of P- and T-axes. These approximate the maximum and minimum compressional stress directions in the region (McKenzie, 1969). As the rose diagrams show, the extensional T-axes have a nearly horizontal average NE–SW trend while the average compressive stress P-axes are nearly vertical with a NW–SE trend. This distribution suggests that the tectonic regime in the study area is dominated by ENE–WSW extension and NNW–SSE normal faulting, compatible with the direction of the activated structure. ENE–WSW extension deduced from the strike of the prevailing T-axes is consistent with the horizontal ground opening vector direction obtained from field measurements at Siamo village (Ganas et al., 2012).

3.3. Spatio-temporal distribution

The temporal distribution of the seismic swarm can be divided in 6 groups that correspond to periods of main/secondary outbreaks in the seismicity (Figs. 12 and 13). Period A (14–22 August 2011) with 170 events, begins with the major $M_w = 4.8$ earthquake of 14 August and spatially concentrated activity at the northern part of the distribution,

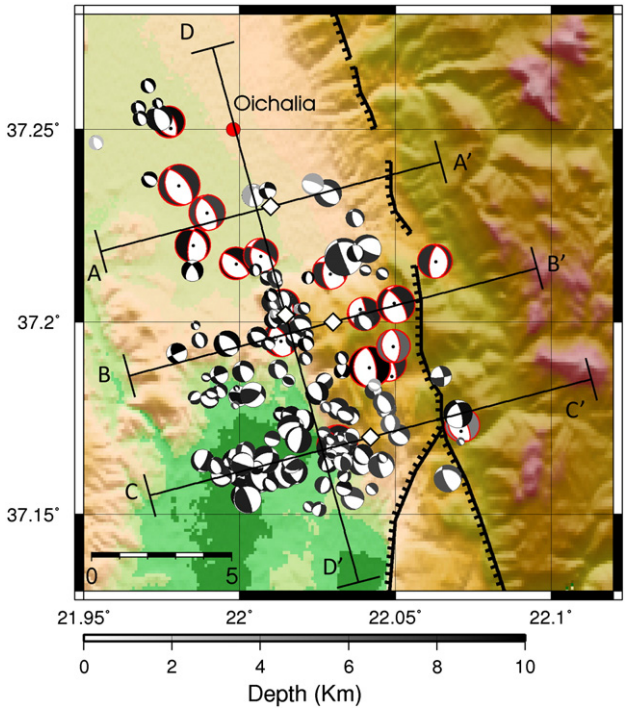

Fig. 9. All 146 focal mechanisms determined in the present study. The size of beachballs is proportional to the magnitude, which ranges between 0.4 and 4.8. Beachballs with solid circles at their centers denote regional MT solutions, while the rest denote P-wave first motion polarities solutions. The profiles AA′, BB′, and CC′, drawn at N75°E direction, as well as profile DD′ drawn at N165°E direction, centered at the white diamond, are used for the focal mechanisms cross-sections of Fig. 10.

involving almost exclusively spatial clusters #1 and #2. Period B (22 August–13 September 2011) with 137 events, is a secondary sequence that follows the $M_w = 4.1$ and $M_w = 4.0$ events of 22 and 23 August, when a more southerly segment of the rupture zone was activated, mostly not only involving cluster #2 but also reaching clusters #3 and #4. The next outbreak (period C: 13 September–9 October 2011) was triggered by an $M_w = 4.6$ event on 14 September and contains several events with $M_L \geq 3.0$. Seismicity within spatial cluster #5 was also recorded during this period, while the activity keeps spreading towards the South. The next three major events of the sequence ($M_w = 4.3$, 4.3 and 4.7, respectively, on 10 October 2011) generated the major outbreak that occurred during Period D (9 October–7 November 2011) with a total of 457 events, not only ranging mainly at the southern portion of clusters #4 and 5 but also reaching cluster #6. During the last two periods (E and F) a couple of spatio-temporal sub-clusters occurred in the northern part (occupying cluster #1), induced by an $M_w = 4.1$ event on 12 November, while the activity in the rest of the rupture zone continues to spread towards the southern end, at the shallower portion of the activated zone.

As far as the 6 largest multiplets are concerned, in the northern and the middle part of the activated zone, two of them (#4 and #5 in Fig. 14) were simultaneously generated at the beginning of the sequence, strongly clustered both in time and space. Later, starting on September 14th and for more than a month, there was sporadic activation of three large multiplets on the southern part, namely #2, #3 and #6 (Fig. 14). The last large multiplet is located in the North (#1 in Fig. 14). It emerged on December 1st after a few pre-shocks, probably triggered by another, smaller spatio-temporal cluster that was activated on November 12th. It is qualitatively different from multiplet #4, which occurred at the beginning of the sequence, as no pair of events with a cross-correlation maximum value over $C_{th} = 0.75$ could link the two of them. The relocated foci of these large multiplets are concentrated in volumes of about 1–2 km diameter, following the general direction and dip of the rest of the swarm's distribution. However, multiplets #1 and #4 appear to be slightly dislocated from the others, mainly because of the gap between these two and multiplet #5.

It is noteworthy that a gradual migration of seismic activity can be observed from the Northern to the Southern part of the rupture zone. Although this is evident from the cross-sections of Fig. 13 it is more clearly demonstrated in the diagram of Fig. 15, which shows the projection of epicenters on a line that passes through the middle of the spatial sequence at N165°E azimuth with respect to the relative origin time (X-axis). The temporal derivative of the thick parabolic curve drawn through the middle of the distribution represents the migration rate. A linear approximation for the average rate of migration of the seismic activity towards the south during the first 80 days is about 80 m/day. At the same time, it appears to ascend to relatively shallower depths in the southern part. Since the first outbreak of 14 August 2011, starting from ~18 August and up to about ~28 October, the seismicity occurs on a migrating active patch, about 6–8 km long (~8 km, roughly represented by the 95% confidence bounds drawn with dashed lines) in the N165°E direction. The occurrence of two small sub-clusters around days ~90 and ~110 (at about 12 November and 1 December) with Y <— 4 km, located in the northern part, likely contributed to the more dispersed distribution of events within the whole length of the rupture zone. The migration speed apparently slows down after day 80, as the seismicity reaches its full expansion, being gradually diminished afterwards.

The thick envelope curve in Fig. 15 corresponds to the distance of the triggering front $r = r(t)$ (Eq. (1)) from the source of fluid infiltration, relative to the time $(t - t_o)$ since the occurrence of the injection, as defined by Shapiro et al. (1997):

$$r(t) = \sqrt{4\pi D(t-t_o) + \gamma_o} \quad (1)$$

starting at $t_o = 6$ days before the origin time of the major event (14 August 2011), with hydraulic diffusivity $D = 1.10$ m^2/s. This is by no means the only plausible solution, as various combinations of D, temporal and spatial offsets can define a satisfactory envelope line. Additionally, the exact time, location and geometry of the fluid injection source are unknown. However, this set of parameters provides an envelope curve for the triggering front with approximately the same slope as the seismicity migration curve. We have also imposed the t_o value so that the source of fluids (y_o) coincides with the projection of the hypocenter of the major event. The same curve mirrored downwards can also be thought of as an envelope of the events occurring NNW of the major earthquake, at the beginning of the sequence, along the same direction.

A wide range of D values has been calculated in other cases worldwide. For the earthquake swarms of 2002 in Mt. Hochstaufen, Germany, a hydraulic diffusivity value of $D = 0.75 \pm 0.35$ m^2/s was measured, with origin times for the fluid intrusion based on intense raining events, while the seismicity was also correlated to precipitation and groundwater increase (Kraft et al., 2006). For the 2001 Agios Ioannis earthquake swarm in Northern Peloponnese, Greece, the migration rate was estimated at 20 m/day for an active fault patch length of ~3 km, propagating up to a distance of ~2 km at shallower parts of the fault surface in 100 days (Pacchiani and Lyon-Caen, 2010). In that case, values of D between 0.08 and 0.20 m^2/s were considered for origin times of diffusion between 88 and 22 days, respectively, prior to the occurrence of the major $M_w = 4.3$ event of 8 April 2001. Temporally variable measurements of hydraulic diffusivity have been carried out by Rigo (2010), for an aftershock sequence of 1996 in Pyrenees, France, with values of D decreasing from 5 to 1 m^2/s for different multiplet families with a common origin time and location of fluid intrusion. In China, gradually increasing average D values between 2.1 and 3.5 m^2/s were calculated for three stages of the aftershock sequence of the 2008, $M_s = 8.0$ Wenchuan earthquake (Liu et al., 2013).

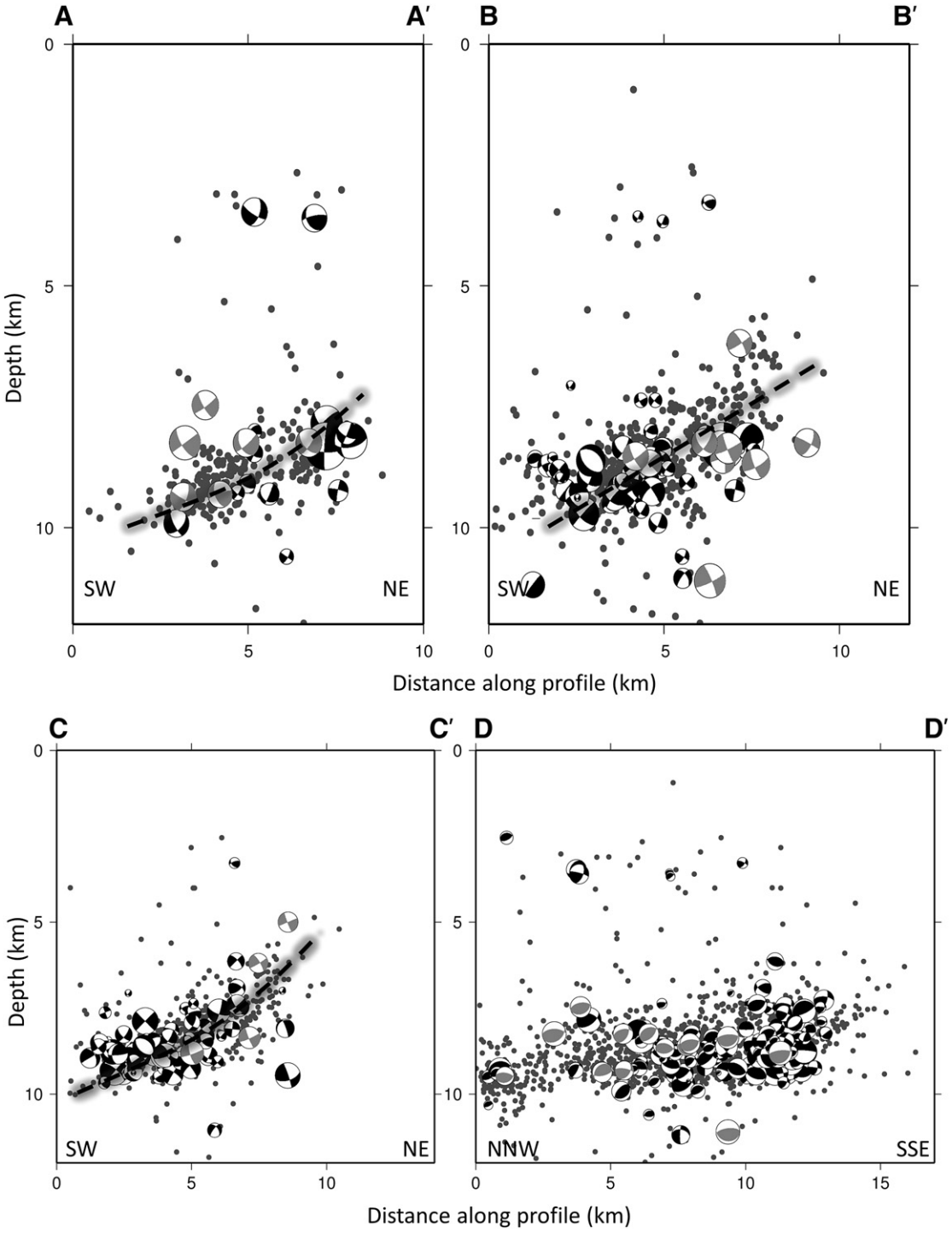

Fig. 10. Focal mechanism cross-sections along profiles AA′, BB′, CC′ and DD′ (Fig. 9). The gray beachballs denote MT solutions derived using regional data, while the black ones denote mechanisms constrained with P-wave first motion polarities. The size of the beachballs is proportional to the corresponding event's magnitude. The dashed lines represent the projection of the inferred fault surface, with a lower dip angle at its deeper portion.

The triggering front model for the migration of seismicity provides evidence that the spatio-temporal distribution of the seismic swarm can be explained by an injection of fluids (Schoenball et al., 2010). Their source is assumed to be close to the hypocenter of the major event of 14 August, starting about a week before its occurrence. It is interesting at this point to note that the NOA database has registered about 120 events between July and August 2011, with epicenters concentrated at the area where the 14 August event occurred. This means that the fluid injection could have started more than a month before $t = 0$. However, under the scope of this study, we have used $t_o = 6$ days to avoid a long extrapolation of the theoretical *rt*-curve.

3.4. b-Value distribution

The tool we used to investigate redistribution of stress, which influences the subsequent swarm evolution, is the spatio-temporal

Table 6
Tabulated source parameters of the major events used for Coulomb stress transfer calculation.

Date	Origin time	Lat (°)	Lon (°)	Depth (km)	*M*	Strike (°)	Dip (°)	Rake (°)	Origin
13/9/1986	17:24	37.11	22.19	5	6.0	201	45	−77	Lyon-Caen et al. (1988)
16/9/2001	02:00	37.24	21.93	10	5.4	130	40	−86	CMT
3/1/2004	00:36	37.17	22.12	12	5.4	211	30	−58	UoA
14/8/2011	01:05	37.23	21.98	8	4.8	165	39	−75	This study

distribution of *b*-values of the Gutenberg–Richter law (Gutenberg and Richter, 1944),

$$\log_{10} N = a - b \cdot M, \tag{2}$$

where *N* represents the number of earthquakes with magnitudes larger than or equal to *M*, and *a* and *b* are constants. The *b*-value of Eq. (2) is of great importance in constraining seismotectonic and hazard analysis because of its dependence on the stress, material heterogeneity and pore pressure (Wyss, 1973). Statistically significant variations of the *b*-value have been reported in laboratory experiments, mines, volcanoes, subducting slabs and along fault zones in foreshock and aftershock sequences, as well as in seismic swarms (Mogi, 1963; Scholz, 2002; Wiemer and Wyss, 2002). When sampling large volumes of the earth's crust, it has been observed that the *b*-values approach unity, which has led to the interpretation of this value as a universal constant (Kagan, 1999). On the other hand, when sampling smaller volumes, such as fault zones, significant deviations have been reported, with the *b*-values varying systematically with respect to the faulting mechanism, thus resembling a stress-meter that measures differential stress (Schorlemmer et al., 2005; Wiemer and Wyss, 2002). In general, the behavior of the *b*-value is inversely proportional to the stress. Low *b*-values are associated with highly stressed asperities (Scholz, 1968), effective stress (Wyss, 1973), foreshock activity and impending large earthquakes while high *b*-values are related to decreased shear stress in aftershock sequences, heterogeneous and complex geological environments, extensional stress regimes, volcanic processes, swarms, pore pressure variations and fault creep mechanisms.

In a previous recent work, Chouliaras et al. (2013), using the NOA catalog locations and magnitude determinations, studied the case of self-triggering of the 2011 Oichalia swarm by investigating the *b*-value distribution across the study area. However, the data included in that catalog contain significant hypocentral uncertainties, hence the authors encourage the elaboration of a more detailed study with the use of improved hypocentral locations of the swarm. We were therefore motivated to perform a complementary analysis using the 1480 relocated events. By applying this, we aim to a certain improvement in the accuracy of the swarm's spatio-temporal characteristics, providing further insight to its triggering and evolution mechanism.

We have determined and mapped the spatial and temporal *b*-value distribution in the Messinia basin using the relocated hypocenter data set and the ZMAP software (Wiemer, 2001). The waveform data recorded at 4 out of the 8 temporarily installed local stations were available in real-time to the NOA acquisition server. These stations were also included in the automatic event-detection scheme, thus improving the detectability of smaller events since 14–20 October 2011. This is evidenced in Fig. 16A which shows the temporal distribution of the completeness magnitude (M_c). An important improvement of M_c can be observed after the installation of the local network, around decimal year 2011.8, compatible with Chouliaras et al. (2013). Another important point regarding the FMD is the increase of the average *b*-value from 0.85 to 1.16, during the second period (Fig. 16B–C).

The increase of *b*-values is further evidenced in Fig. 17A, which shows the temporal evolution of *b* during the 2011 swarm using the entire earthquake catalog including 1480 relocated events. In Fig. 17A, a number of 100 events and 100 bootstraps per *b* estimate were used. The standard error of the mean *b* values estimated by the bootstrap

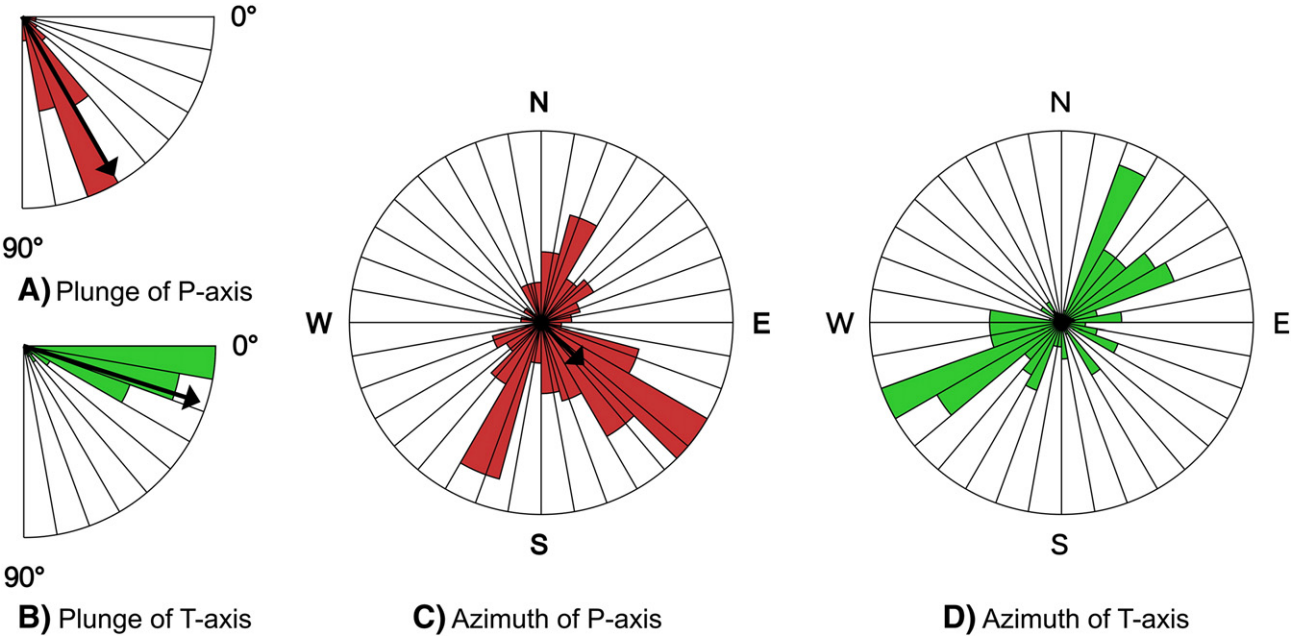

Fig. 11. Geometry of P- and T-axes of focal mechanism solutions obtained in this study. Plunge angles are shown in (A) and (B) for P- and T-axes, respectively, with 0° indicating the horizontal direction and 90° the vertical one. Black arrows show the average solution (the length of arrows is proportional to the homogeneity of the corresponding observations): 60° for P-axes and 19° for T-axes. The distribution of azimuths is presented in (C) and (D) for P- and T-axes, respectively. Arrow in panel (C) corresponds to the average azimuth N135° of the P-axis. Arrow in panel (D) has zero length, since T-axes are almost horizontal; those are trending roughly in a NE–SW direction.

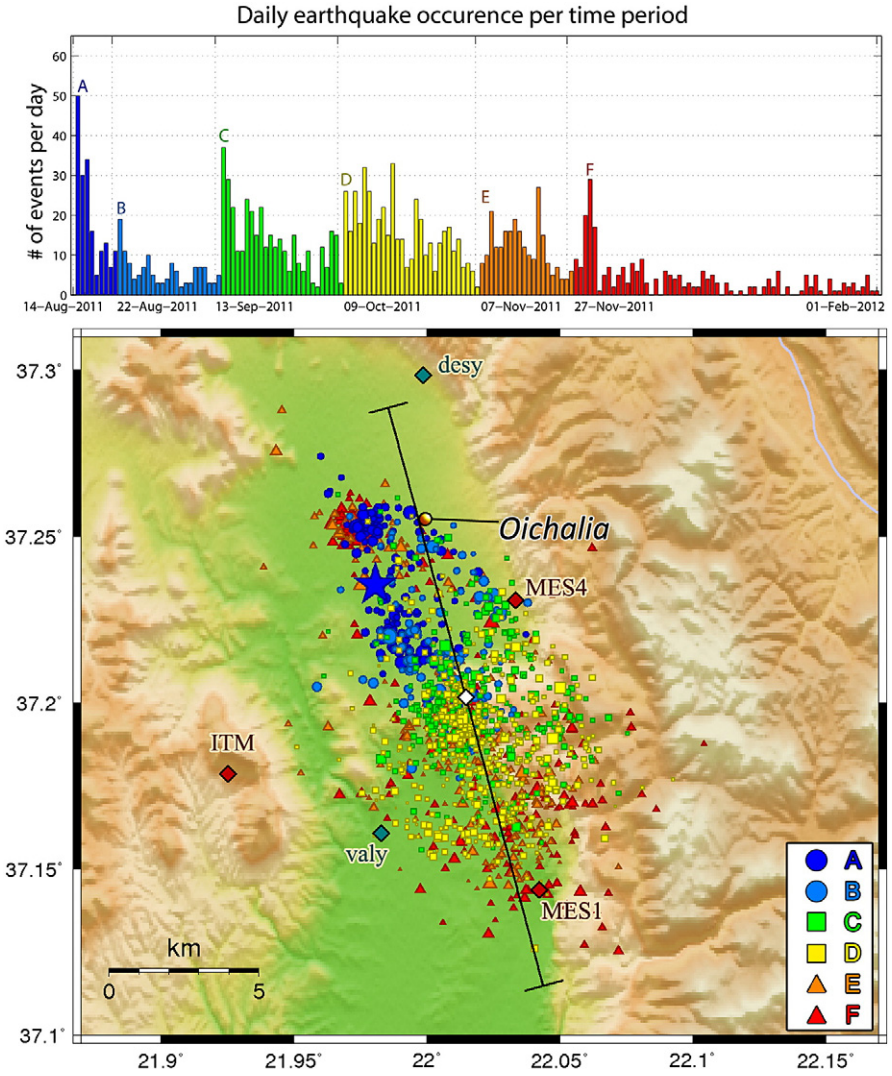

Fig. 12. Map of the temporal evolution of the relocated events with different colors representing the six consecutive periods in which the seismic swarm sequence has been divided. The embedded histogram shows the daily number of earthquakes per time-period (A–F). The line drawn at N165°E azimuth, centered at 37.2018°N, 22.0148°E (white diamond) is used for the cross-sections of Fig. 13 and the spatio-temporal projection of Fig. 15. The star denotes the major event of 14 August 2011. Local stations are represented by triangles.

method is calculated using the formula of Shi and Bolt (1982). Estimates correspond to the end-time of each moving average, hence the calculated *b*-values represent the conditions right before the absolute occurrence time of the last event in each window. Temporal distribution of *b* was also calculated using a lower magnitude threshold of 1.6, equal to the average M_c of the period prior to the installation of the local network, adopting thus homogeneous sample data. A number of 150 events per *b* estimate were used at each one of 200 bootstrap solutions with overlapping. As it can be seen, the *b* pattern between the two panels is consistent, hence we can imply that the overall *b*-value increase during the evolution of the swarm is not an artifact due to the catalog completeness, but reflects the physical properties of the seismic volume. As it can be seen from both panels of Fig. 17, the average *b*-values range mainly between 0.7 and 1.5, in agreement with the corresponding values of seismic swarms in continental rifts (Ibs-von Seht et al., 2008). Significant variations are observed throughout the sequence, which correlate with the occurrence of major events (Fig. 17). Inter-seismic periods (ellipses in Fig. 17A) likely represent discrete phases of the swarm's evolution (capital letters above the ellipses in the same figure).

As the distribution implies, the first phase during 14/8/2011–14-9/2011 (A) is characterized by low *b*-values. This phase started with the occurrence of the major event on 14/8/2011 at the northern part of the sequence and propagated to the south (spatio-temporal clusters A and B, Fig. 12). The second phase (B) started on 14/9/2011 with a major $M_w = 4.6$ and is characterized not only by generally high *b*-values, but also by significant transitions of *b*. Phase B involves the largest spatio-temporal clusters C and D and further migration towards the south (Fig. 12). A minimum value observed on 10/10/2011 correlates with the occurrence of 3 major events (on 10 and 11 October), marking the end of the first part of the phase (B_1) and the initiation of B_2. The latter is characterized by the largest variations of *b* during the swarm, including two local minima. The first, at the end of October 2011, is not correlated with any major event. The second minimum of B_1 phase on 12/11/2011 correlates with a major event of $M_w = 4.1$ that occurred at the northern part of the epicentral area, in the vicinity of the initiation of the crisis. This is the beginning of phase C, which presents smoother variations of *b*-values towards the universal constant of unity, signifying the end of the activity around 31/12/2011.

The seismicity during phase C is spread throughout the epicentral area, as spatio-temporal clusters E–F indicate (Fig. 12). However, it is noteworthy that the results displayed in Fig. 17 suggest that the observed variations of the Frequency–Magnitude Distribution (FMD) are related to a temporal shift of the seismic activity from volumes of low

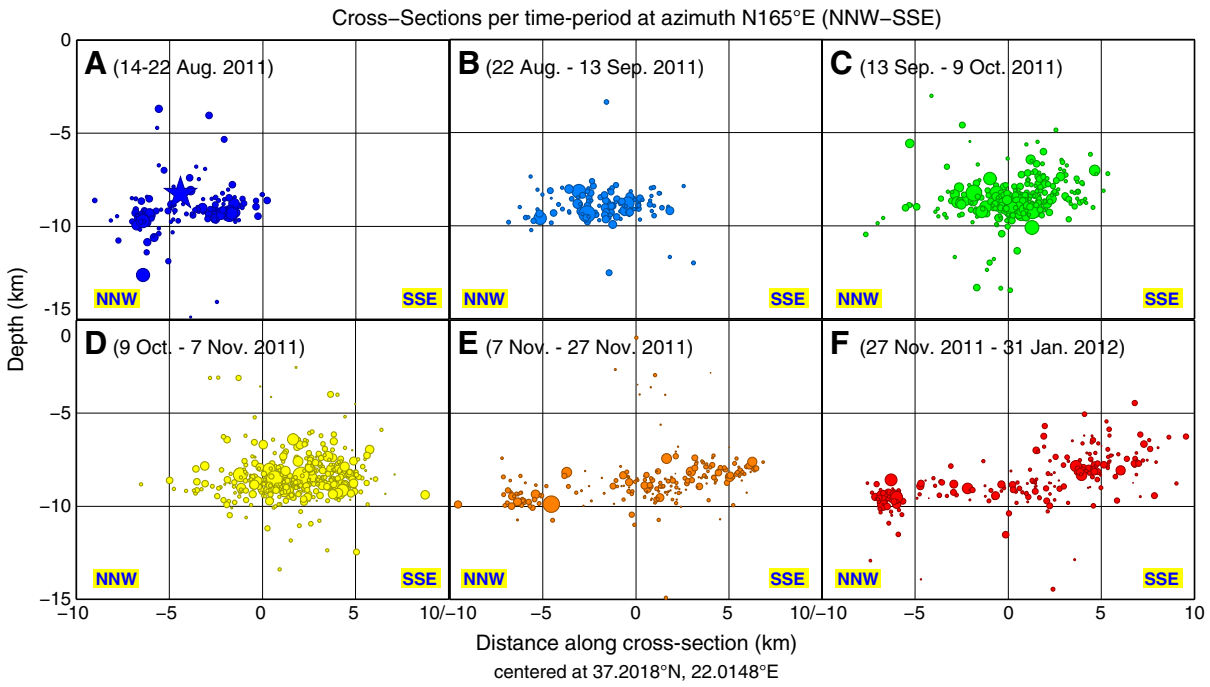

Fig. 13. Cross-section of the events at N165°E direction (NNW–SSE), centered at 37.2018°N, 22.0148°E (see Fig. 12) for consecutive time windows. Panels A–F represent the 6 periods that the temporal distribution was divided at (same as in Fig. 12): A) 14–22 Aug. 2011, B) 22 Aug.–13 Sep. 2011, C) 13 Sep.–9 Oct. 2011, D) 9 Oct.–7 Nov. 2011, E) 7 Nov.–27 Nov. 2011 and F) 27 Nov. 31 2011–31 Jan. 2012. The star in period A denotes the major event of 14 August 2011.

background *b*-value to neighboring volumes with higher values. The migration of seismicity towards SSE is indeed demonstrated by the spatio-temporal cluster analysis. To investigate possible association of the FMD with stress variations around asperities on the fault, we proceeded with mapping the spatial distribution of *b*-values.

The technique of mapping *b*-values with ZMAP is described in detail by (e.g.) Wiemer (1996), Wiemer and Benoit (1996), Wiemer and Wyss (1997). Accordingly, in this work, *b*-values were estimated at every node of a densely spaced grid of overlapping volumes in order to provide a natural smoothing of the results, using the *n* nearest events. The seismic volume was divided into cylinder-shaped sub-volumes of radius *R*. The nodal separation was 0.01° in map-view and 0.5 km in cross-sections. Each overlapping sub-volume (cylinder) has a constant radius $R = 4$ km, containing $n = 80$ events. Several tests were performed compiling *b*-value maps with constant *R* and varying *n*, resulting in only marginal differences in the spatial pattern. The *b*-values were calculated using maximum-likelihood estimates (Bender, 1983) extending from the magnitude of completeness, M_c, to the maximum magnitude in the set of data. Since M_c can vary as a function of hypocentral location, it was estimated separately for each sub-volume by adopting the maximum value of the derivative of the FMD (Westerhaus et al., 2002).

Resolution tests, regarding the spatial sampling density of the analyzed volume and the standard deviation of *b*-value estimations (<0.1) (Fig. 18), show that our data set can adequately depict the spatial seismicity rate variations using the considered nodal parameterization. The calculated *b*-values are only displayed in areas sampled by $n = 80$ events, as shown in panels A, B and D of Fig. 18. Panel C in Fig. 18 shows that the density of earthquakes is such that the sampling radius is about $R = 4 \pm 1$ km for most nodes if $n = 80$.

The spatial distribution of *b*-values calculated from the 1480 relocated events of the 2011 swarm is presented in Fig. 18A. The lowest values ($0.6 \leq b < 1$) are found in the northernmost part, the epicentral area of the initiation of the swarm with the major shock on 14/8/2011. Based on the correlation of low *b*-values with high ambient stress (Wiemer and Wyss, 1997), we can assume that the events involved in these calculations have occurred in a highly stressed area, even after the major shock. Two patches of normal to moderate *b*-values (1–1.3) have been found at the central-western and the southern patch of the fault. The first is related to the later major outbreaks that occurred during 14 September–12 November 2011, characterized by several events with $M_L \geq 3.0$, as depicted in Fig. 17. The second correlates with the southern termination of the rupture zone, activated after 12 November 2011. Hence, we can define two phases of temporal distribution of *b*-values. A low *b*-value phase during 14 August–9 October 2011, related mostly to the northern part, and a normal to moderate *b*-value phase thereafter, mostly involving the southern part. Translating to ambient stress, we can suggest that the northern part of the seismogenic volume, despite hosting the largest part of co-seismic slip during the swarm, still accumulates high stress, which is rather unusual, as areas of large slip release correlate with high *b*-values (Wiemer and Katsumata, 1999). Therefore, the northern patch may constitute an asperity capable for a future earthquake. However, an aseismic crustal stress relaxation mechanism, perhaps related to fluid circulation across the rupture zone, might be involved, increasing the effective stress and, consequently, decreasing the *b*-values. A concurrent seismic afterslip translation to the south, implied by the spatio-temporal distribution of both *b*-values and earthquake clusters, could have produced the second phase of the swarm, around 14/9/2011. Therefore, an Epidemic Type Aftershock Sequence (ETAS) model (Hainzl and Ogata, 2005) is inferred. According to ETAS, each event within a swarm is capable to induce other events, in other words its own aftershocks, driving the seismicity, redistributing stress within the seismogenic volume. The latter is further implied by the spatio-temporal *b*-value distribution, which demonstrates both expansion of epicenters and increase of seismicity rates towards the SSE (Fig. 19).

In order to explore volumes of significantly increased or decreased *b*-values, associated with possible un-ruptured asperities along the fault zone that are capable to produce forthcoming earthquakes, differential mapping of *b*-values was performed, regarding periods of the 3 distinguished temporal phases of the seismic swarm. Differential maps were compiled for pairs of different temporal phases using ZMAP software, with $n = 80$ earthquakes per sample, applying constant-sized volumes ($R = 4$ km) to allow the comparison of the FMD at each

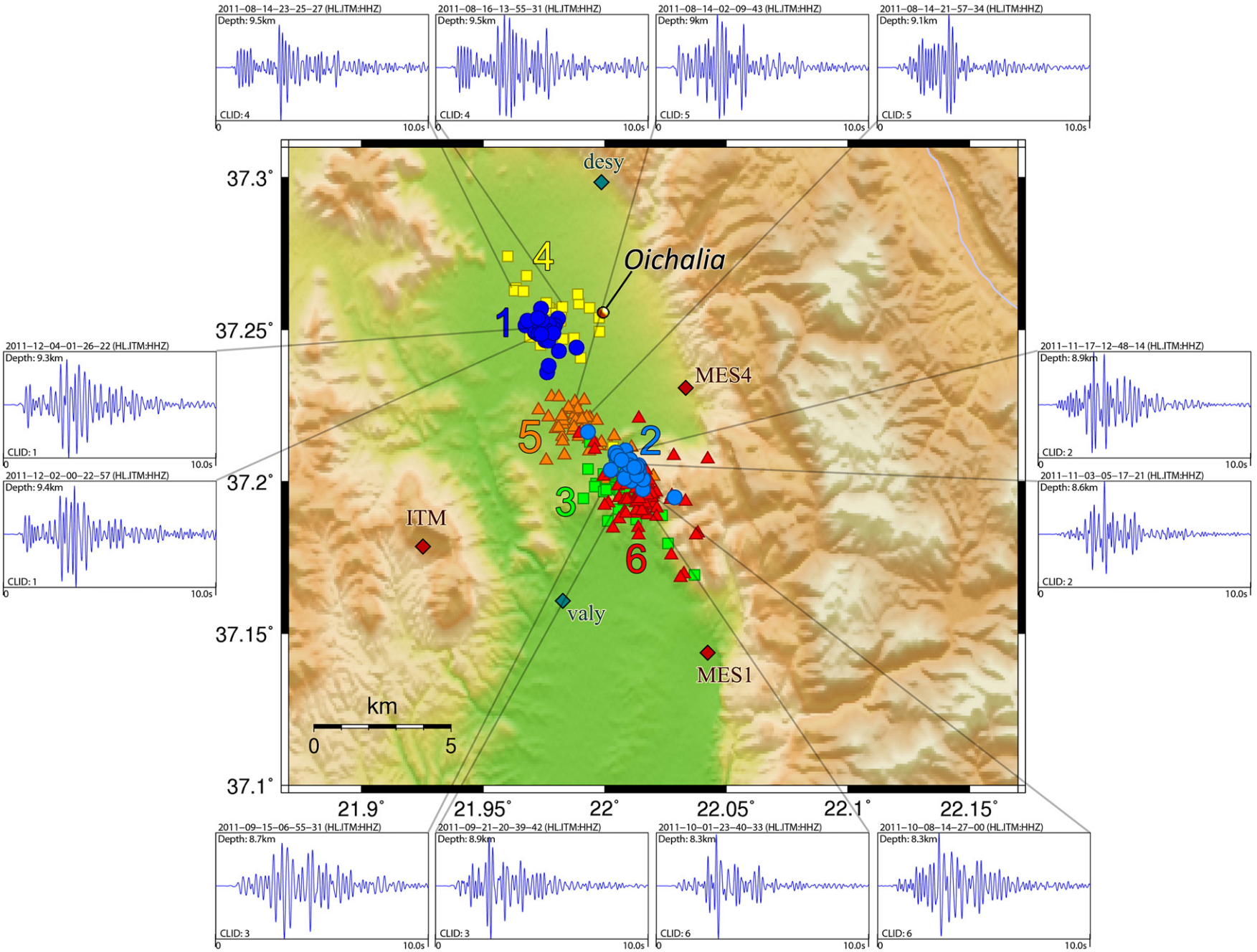

Fig. 14. Map of the relocated epicenters for the 6 largest multiplets with size ≥20. Different colors and shapes represent different multiplets, labeled with numbers from 1 to 6. Waveforms in the periphery of the figure depict the vertical component of the permanent station ITM for pairs of events that belong to the same multiplet. The waveform panels also include information about the origin time and depth of the corresponding event. Local stations are marked as diamonds.

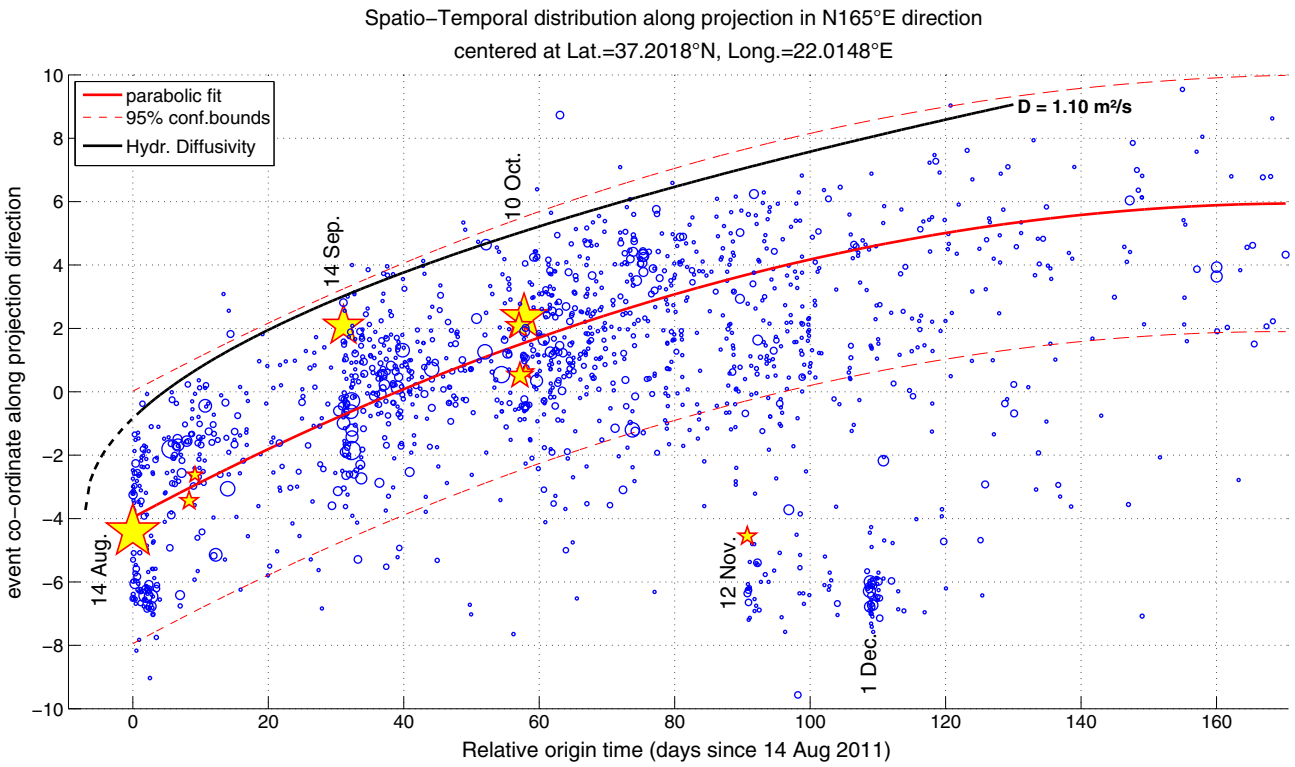

Fig. 15. Spatio-temporal diagram of the swarm activity. The vertical axis represents the projection of epicenters along the line shown in Fig. 12, centered at $Y = 0$ or 37.2018°N, 22.0148°E (white diamond in Fig. 12), drawn at N165°E azimuth, with $Y = -10$ km being at the NNW end (37.2887°N, 21.9855°E) and $Y = 10$ km being at the SSE end (37.1149°N, 22.0440°E). The horizontal axis denotes the relative origin time measured in days since 14 August 2011. The solid curve is a parabolic-fit estimate of the mean migration rate of seismicity along the N165°E direction with a mean slope of ~80 m/day for the first 80 days. Dashed lines mark the 95% confidence bounds with a width of about 8 km. Stars denote events with $M_w \geq 4.0$ (see Table 4). The envelope curve corresponds to the position of the triggering with the source of fluid infiltration at the same position as the 14/8 event hypocenter, starting at $t_o = 6$ days before the origin time of the major event and defined for hydraulic diffusivity $D = 1.10$ m^2/s.

node between two different phases (Fig. 20). According to Wiemer and Wyss (2002), for sample sizes $n = 80$ variations of b of the order of 0.3 ($\Delta b \geq 0.3$) can be established with significance and hence, we only discuss analogous Δb contrasts. Small increase is implied at the northern part especially during phase C and a larger decrease (0.3–0.4) at the southern part, during phases B and C. This means that change in b has occurred near the patches of largest slip. The AB–C differential map indicates that b-values in the northern part, while being low overall (Fig. 19), have in fact been increased during phase C (Fig. 20, lower panels). This change is due to the occurrence of two small spatio-temporal clusters in phase C, which, evidently, relaxed the stressed area.

3.5. Coulomb stress changes

Seismic slip causes redistribution of static stress, which may in turn accelerate or delay the occurrence of other strong seismic events. Sites with increased probability for future earthquakes may be predicted based on the Coulomb failure criterion; events are more likely to occur where Coulomb stresses have risen (King et al., 1994). To understand whether the 2011 swarm was induced by static stress load and if the foci distribution follows a relevant pattern, we evaluated the Coulomb stress changes upon the fault plane, considering all major earthquakes that have occurred in the broader region since the most severe 1986, $M_s = 6.0$, Kalamata earthquake. The parameters of the earthquakes used in the calculations are listed in Table 6. The estimation of Coulomb stress changes was performed with the Coulomb 3.3 algorithm (Toda et al., 2011), assuming a Poisson's ratio of 0.25 and a shear modulus of 30 GPa. The Coulomb stress change on a specified fault is independent of regional stress but depends on the fault geometry, type of slip, and the coefficient of friction (King et al., 1994). Since no slip distribution models were available, unilateral and uniform ruptures were considered in all cases. Our analysis relied solely on earthquake data, thus it does not provide any estimate of the total stress amplitude, e.g. the pre-existing shear stress. Furthermore, we did not account for non-elastic, aseismic processes, like post-seismic visco-elastic relaxation due to afterslip. These effects have been shown to increase the overall stress (Pollitz and Sacks, 1992), in which case our stress change calculations may be slightly underestimated. The analysis of such parameters is beyond the scope of the current research, as it would require a variety of additional experimental constraints, like continuous GPS measurements.

Stress changes along Receiver Faults (RF) are presented in Fig. 21, with "stress-loaded" areas (where slip is accelerated) and relaxed areas (where slip is delayed). Concerning the effective friction coefficient (μ'), which is directly proportional to the amplitude of the induced stress across the RFs, a relatively low value ($\mu' = 0.40$) was adopted. This is in accordance with Floyd et al. (2010), who suggest that the normal-fault systems throughout the Aegean, aligned roughly perpendicular to the principal axes of elongation in the geodetic velocity field, require that the upper crust accommodates a coherent strain rate field with relatively low effective friction coefficient on faults (<45%). Coulomb stress transfer computations were performed on a RF with strike, dip and rake assumed by averaging the MT solutions of Table 4 (Strike = 175°, Dip = 37°, Rake = −72°).

As presented in Fig. 21, only the southernmost portion of the 2011 hypocenters is located within positive stress lobes of the 1986, $M_s = 6.0$ Kalamata earthquake. The Oichalia seismic swarm was initiated with an $M_w = 4.8$ event on 14 August 2011 at the northern part (latitude ≈ 37.23°), where no Coulomb stress was transferred. We can therefore suggest that the epicentral area of the 2011 activity was not affected by the 1986 event. Regarding the cases of the 2001 and 2004 earthquakes (Table 6), both could have accelerated the occurrence of the 2011 seismic swarm, as it is included within positive lobes of Coulomb stress.

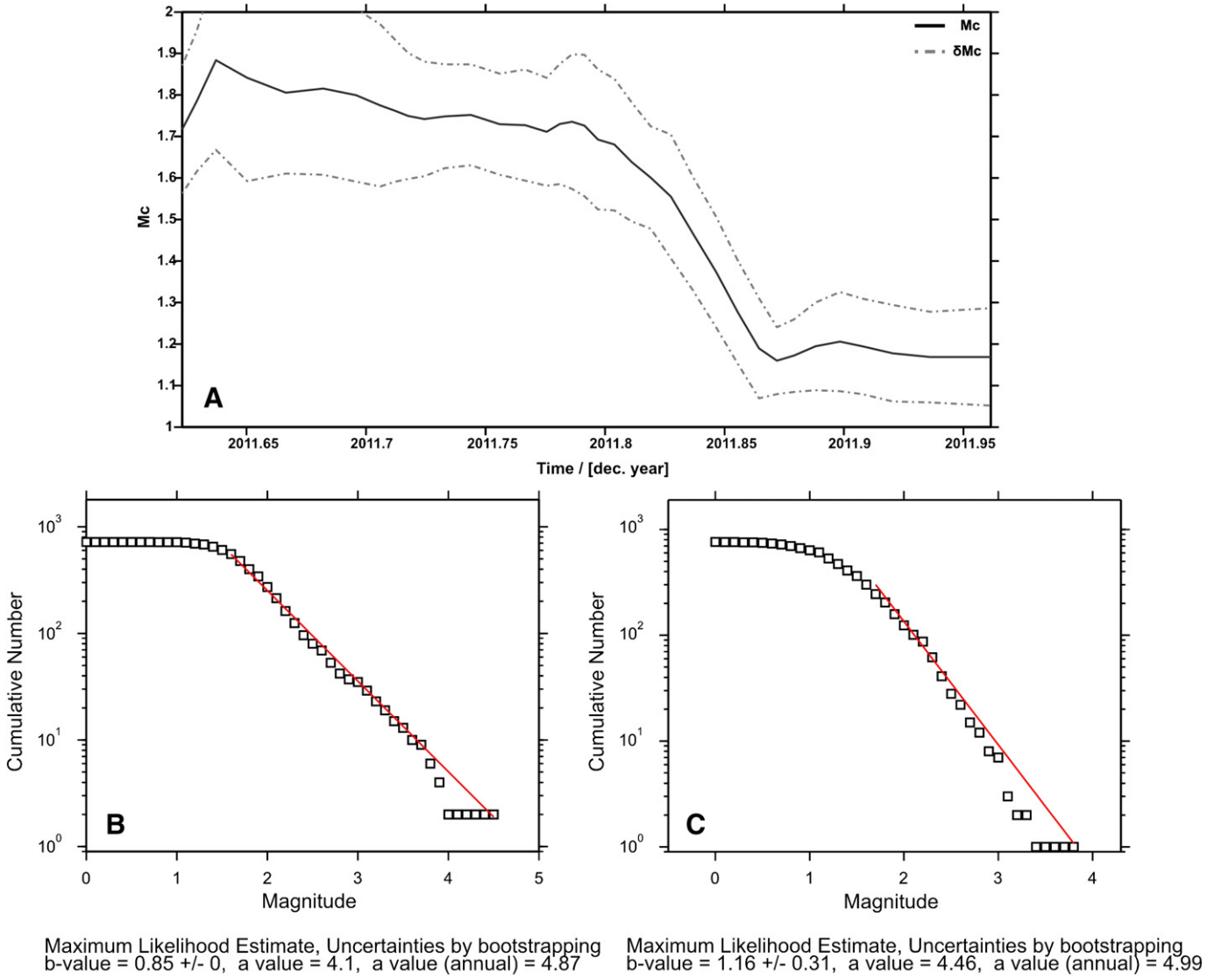

Fig. 16. (A) Temporal distribution of the completeness magnitude using ZMAP. A sample of 150 events, 200 bootstrap solutions and overlapping were considered. δM_c is computed using the Shi and Bolt (1982) formula. (B and C) FMDs prior to and after the installation of the local network, respectively.

Lastly, we examined the case of the 14 August 2011 major shock ($M_w = 4.8$). As with the other cases, the size of the maximum induced stress is small, ~0.5 bars. At the bottom-right panel of Fig. 21, a NW–SE cross-section, parallel to the inferred 2011 fault zone, shows that the temporal clusters 'A' and 'B' (period 14 August–13 September, Fig. 12) are located within the relaxed area of the initiating event, below the stress-loaded zone, which is restricted between 7 and 9 km depth.

Coulomb stress calculations were performed using the strong event of Methoni on 14-02-2008 (36.30° N, 21.69° E, depth = 35 km, $M_w = 6.7$, NP1 (strike = 290°, dip = 16°, rake = 89°)) showing that this recent event did not affect the 2011 epicentral area. Furthermore, calculations employing regional stress were also performed resulting negligible stress changes as expected. It is worth to mention that the small regional stress is in association with the regional strain (1–3 mm/yr) as GPS measurements over an Aegean reference frame indicate (Fig. 1) (Vernant et al., 2014).

The amplitude of the induced stress in the epicentral area was estimated in all cases at about 0.5 bars, just a fraction of the stress drop of an earthquake. Even such weak stress transfer values may be associated with possible earthquake triggering and significant changes in the seismicity rate (Stein, 1999). Seismic activity is expected to increase where additional stress is accumulated (aftershocks) and decrease where the stress drops. To investigate possible seismicity rate changes in the study area, induced by major shocks in the broader area, we analyzed the NOA instrumental catalog during 1964–2007 using the ZMAP software (Wiemer, 2001). We excluded the era after 2007 because the reconfiguration and upgrade of the HUSN have changed the completeness magnitude of the catalog, therefore a direct comparison with the previous period is not feasible. Fig. 22 shows the significance of the seismicity rate change (over 5%) within the 2011 epicentral area. Significant changes are observed only during the 1986, $M_s = 6.0$ Kalamata earthquake and the 2001, $M_w = 5.4$ earthquake that occurred in the vicinity of Oichalia prefecture. No significant post-seismic seismicity rate changes were inferred. This potentially shows that there has been stress shortage in the study area. Hence, an external mechanism of aseismic forcing seems to be required to critically load the focal area and trigger earthquakes (Hainzl et al., 2012; Horálek and Fischer, 2008). This is likely the case when pressurized fluids are involved, which increase the pore pressure and reduce the friction coefficient, bringing the fault to the limit of its stability.

Tectonic forcing, when assuming a first-order approximation of the regional fault slip rate between 0.1 and 2–3 mm/yr (Armijo et al., 1992), is expected to be negligible on the considered time span of 25 years (1986–2011) in the study area. Hence, we suggest fluid

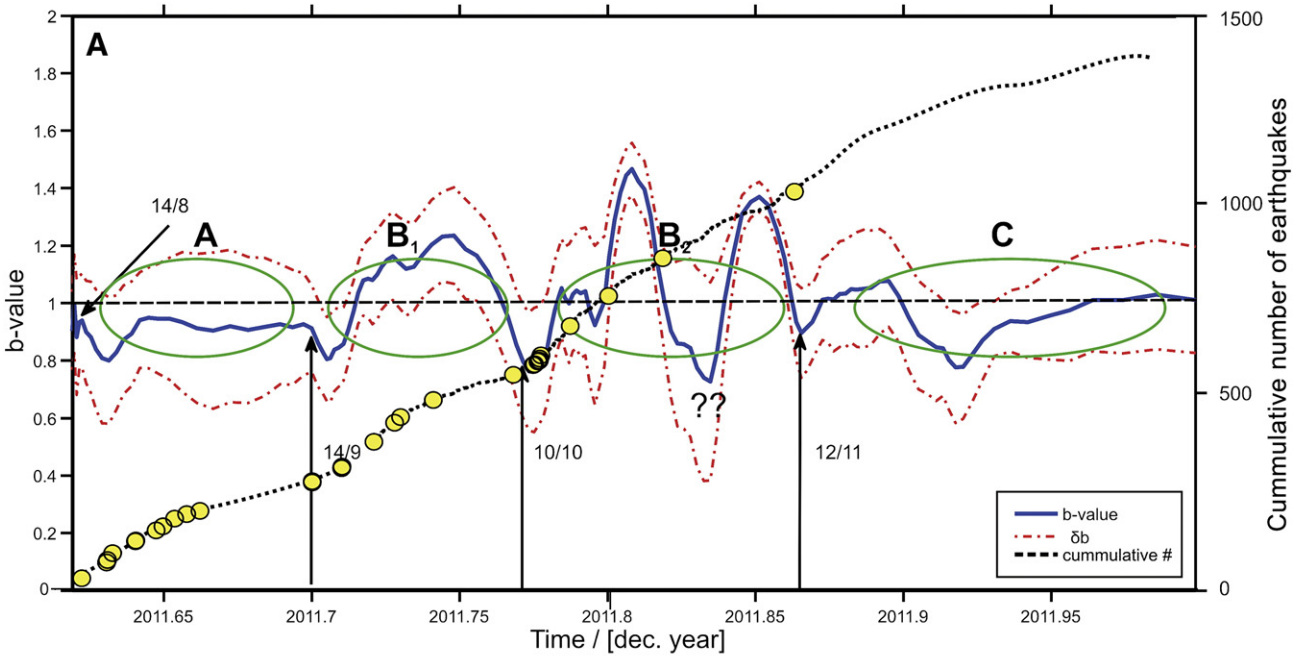

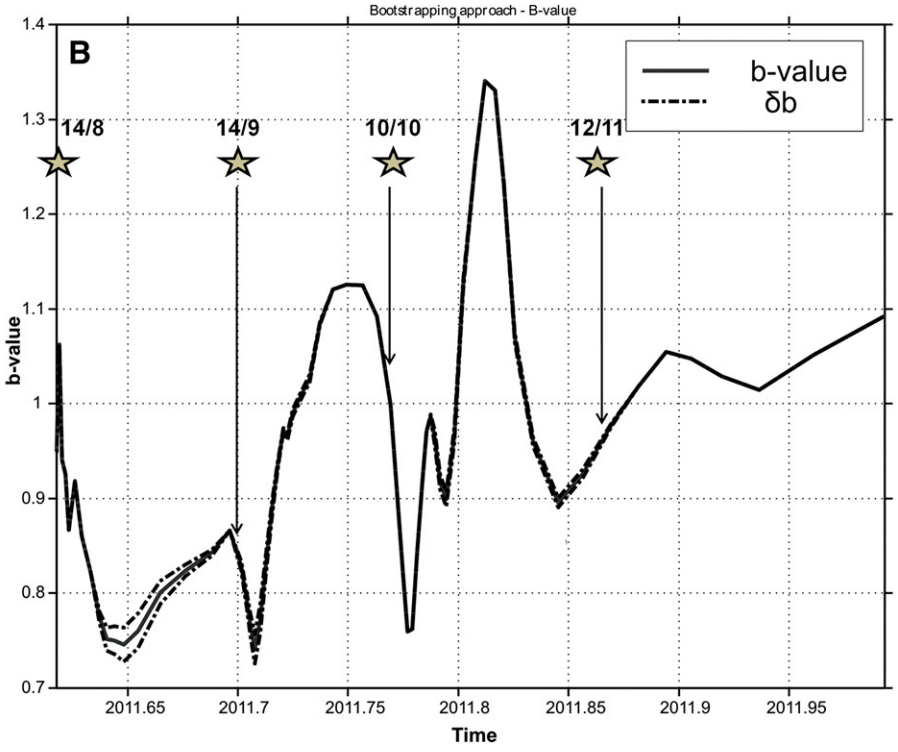

Fig. 17. (A) Triaxial diagram showing the frequency of earthquakes (right axis) and the distribution of *b* (left axis) with respect to the origin time of the last event in the sliding window during the Oichalia sequence (14/8/2011–31/12/2011) using the entire catalog. Circles represent earthquakes with $M > 3.0$. The dashed line denotes the cumulative number of events with time (right axis). Ellipses define inter-seismic periods marked by the occurrence of major earthquakes and the variations of the parameter *b*. Letters at the top of ellipses denote discrete phases of the sequence. Arrows show the date of occurrence of major events correlated with the initiation of sub-phases. (B) Temporal *b*-value distribution using a magnitude threshold ≥ 1.6, equal to the average M_c of the catalog prior to the installation of the local network using 200 bootstrap solutions. Stars denote major events. *δb* is the standard error of the mean *b* bootstrap estimates.

intrusion to be the aseismic loading process, leading to increased pore pressure within the seismogenic rock volume, increasing thus, the effective stress on the fault plane. This might be interpreted by fluid translation prior to the 14 August major event at the deeper part of the seismogenic zone, triggering its occurrence and, consequently, the first spatio-temporal cluster of the swarm (Fig. 15).

4. Discussion–conclusions

In this paper, we present results from the analysis of the dynamics and the spatio-temporal evolution of the Oichalia (SW Peloponnesus) swarm. This was initiated on 14/8/2011 with an $M_w = 4.8$ event and was followed by a large number of aftershocks, several of which having

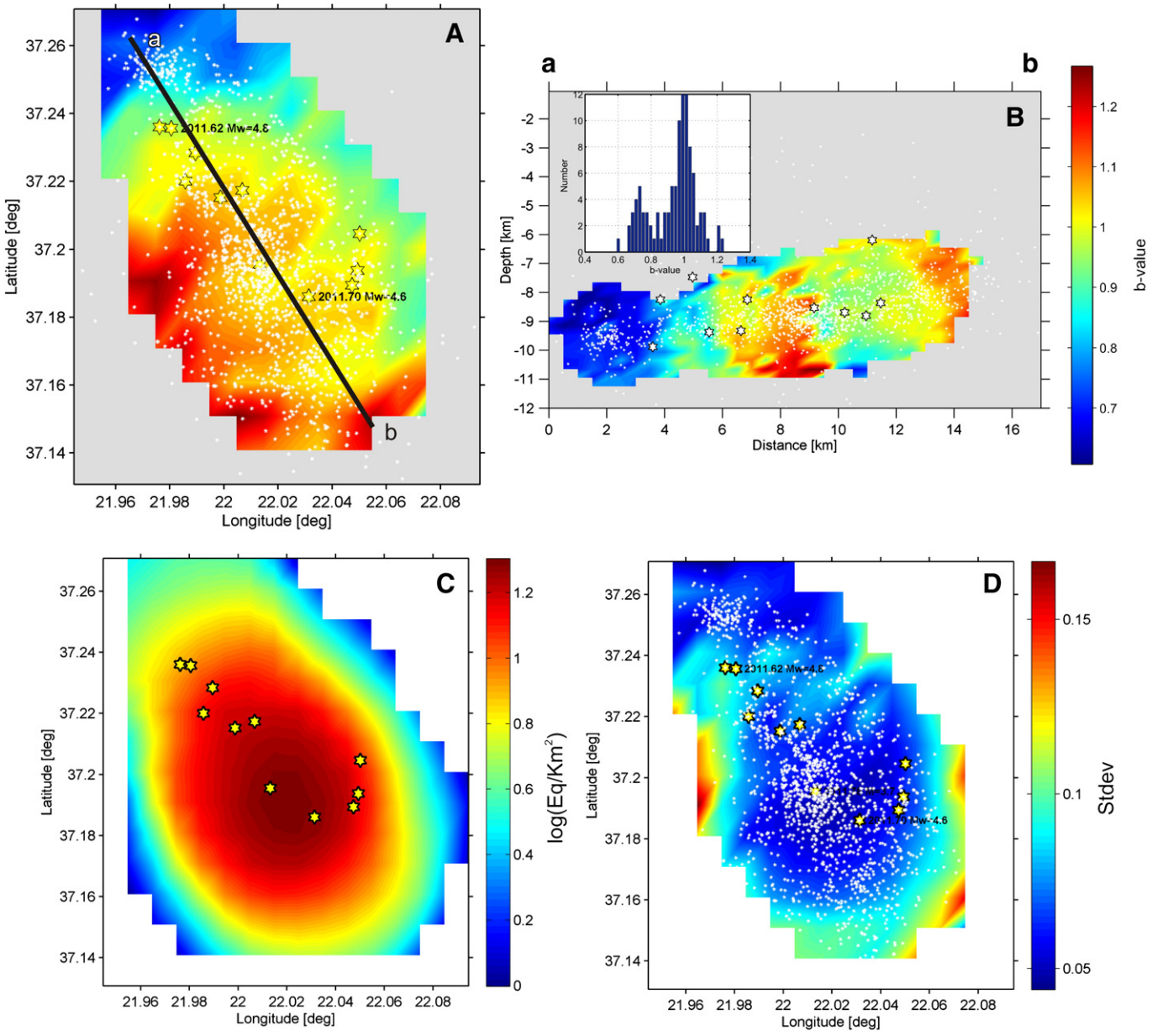

Fig. 18. (A) *b*-Value map for all 1480 relocated earthquakes during 14/8/2011–31/12/2011. The number of earthquakes per sample is $n = 80$, the nodal separation is 0.01° and the radius of the vertical cylindrical sample volumes is $R = 4$ km. (B) *b*-Value cross-section along the *ab* profile shown in panel A. The nodal separation is 0.5 km at both *x* and *y* directions and the radius of the cylindrical sample volumes is $R = 2$ km. The inset histogram shows the distribution of *b*-values. (C) Sampling density, as a measure of spatial resolution of the mapping procedure. (D) Standard deviation of spatial *b*-value determinations. A, B and D panels present areas sampled by $n = 80$ by overlapping sub-volumes of constant $R = 4$ km. Panel C shows the radii necessary to cover the study area. White symbols denote earthquakes and stars represent larger earthquakes with $M \geq 3.5$.

$M_w > 3.5$. Our scope was to assess the dynamic processes of the rupture zone, which provide crucial constraints for the hazard of the seismically prone area of SW Peloponnesus. For this, various techniques and comprehensive analyses were employed. The accurate event location of the 2011 earthquake swarm was made possible using waveform data from both the regional HUSN and a temporary local network, which increased the resolution of the seismicity image. We managed to locate 1615 events with magnitudes ranging 0.4–4.8, using an optimum 1-D average P-wave velocity model and V_p/V_s, which minimized hypocentral errors (Table 1). The obtained hypocentral parameters were further improved by applying a double-difference relocation algorithm (HypoDD) using: (a) the optimized travel-times obtained by HYPOINVERSE with the incorporation of the new local 1-D velocity model, (b) differential P- and S-wave travel-times obtained by waveform cross-correlation on pairs of repeating earthquakes. In total, 1480 events were successfully relocated (about 90% of the swarm) oriented roughly NNW–SSE, compatible with the ground tensile cracks observed at Siamo village (Ganas et al., 2012). Focal depths vary between 3 and 14 km, with an average depth of about 8.7 km. The spatio-temporal cluster analysis of the swarm showed that it follows a NNW–SSE trend with time, towards a large seismogenic zone which produced the 13 September, 1986, M_s(NOA) = 6.0 destructive earthquake.

The geometry of the nearby recording stations allowed the determination of 146 focal mechanisms, with 128 of them constrained using P-wave first motion polarities and 18 using regional moment tensor inversion solutions. Most of the focal mechanisms are characterized by dip-slip normal faulting. Several of them contain a significant strike-slip component and a few appear to be reverse, located mainly at the southwestern part of the epicentral area. Both the spatial distribution of the relocated seismicity and the focal mechanisms reveal that the activated zone has a length of ~18 km. It is a low angle dip-slip normal structure, trending NNW–SSE and dipping ~32° SSW. The average T-

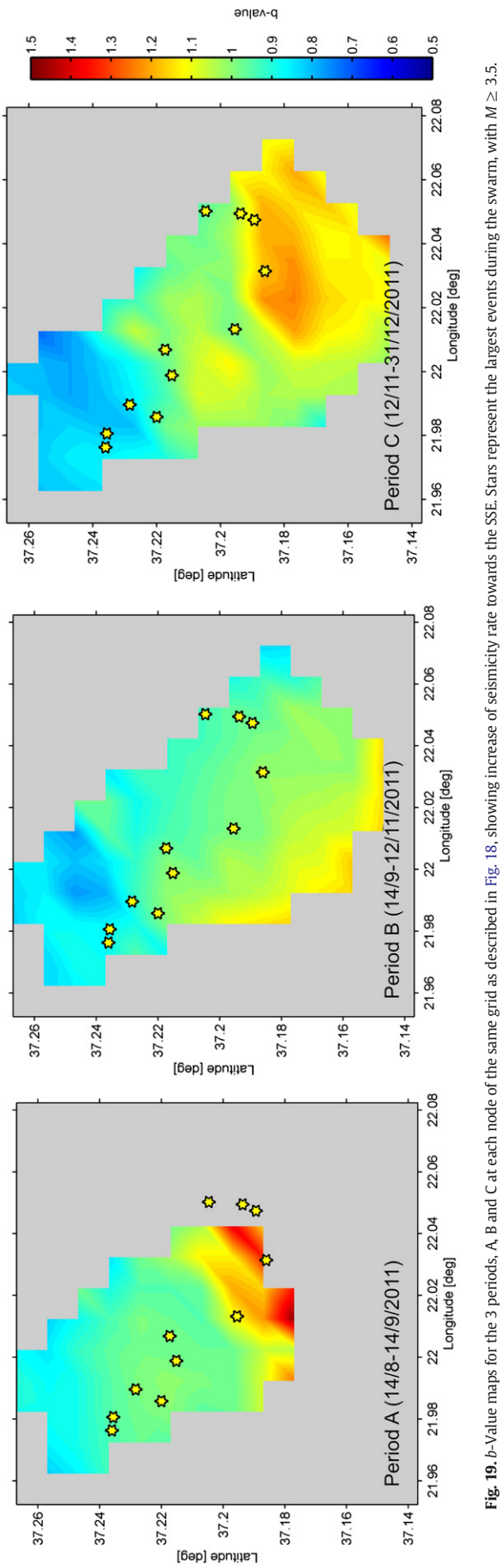

Fig. 19. *b*-Value maps for the 3 periods, A, B and C at each node of the same grid as described in Fig. 18, showing increase of seismicity rate towards the SSE. Stars represent the largest events during the swarm, with $M \geq 3.5$.

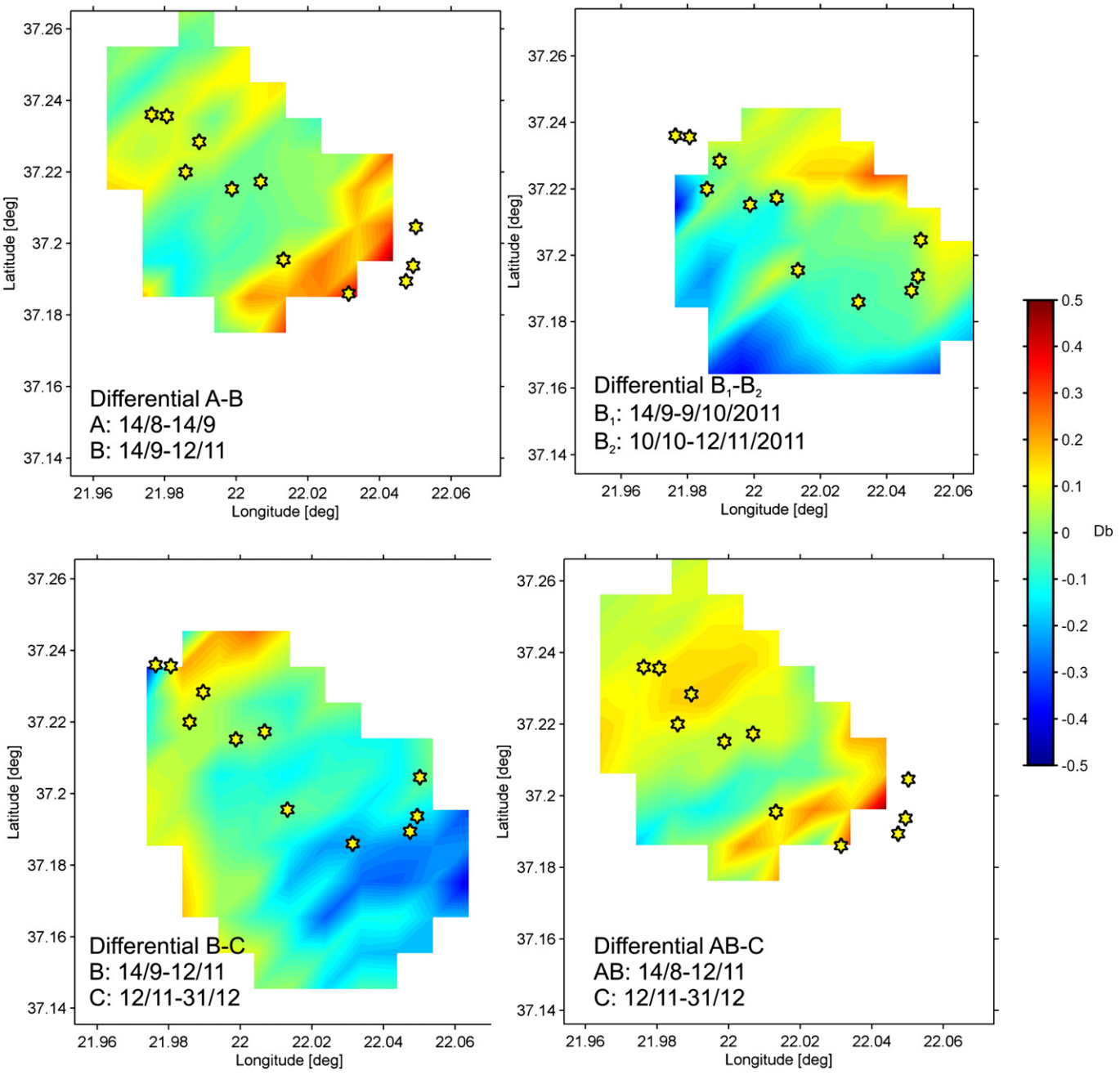

Fig. 20. Differential *b*-value maps for pairs of discrete seismicity periods A, B and C at each node of the same grid as described in Fig. 18, showing volumes of increased or decreased b-value.

and P-axis orientations are ENE–WSW and WNW–ESE, while their plunge is 19° and 60°, respectively. The trend of the elongation axes is compatible with results deduced from seismological (Hatzfeld et al., 1990; Lyon-Caen et al., 1988; Papoulia and Makris, 2004), morphotectonic (e.g. Armijo et al., 1992) and GPS observations (e.g. Floyd et al., 2010).

Regarding the geometry of the activated structure during the 2011 seismic sequence, the average dip of the hypocenter distribution is roughly 20° WSW, while the computed focal mechanisms present a steeper average dip of 42° WSW. Following each of the dip angle configurations, two scenarios are potentially probable: (A) Taking into consideration the low-angle of 20° WSW, a major rupture plane is defined, which, if extrapolated to the surface, is situated some 12 km east of the swarm, apparently projected within an area dominated by the Alpine basement formations and the core of the tectonic horst north of Taygetos Mt. The hypothetic fault should lie along the western ramps of Taygetos Mt. (Fig. 23), (B) Taking into account the focal mechanism average dip of 42° WSW, we could presume that more than one structures are involved, interacting with each other, forming a complex fault network which is compatible with the NW–SE striking and west dipping normal fault observed at the eastern flanks of the Upper Messinia basin. The activation of numerous small-scale synthetic

Fig. 21. Left: Coulomb stress transfer due to the major events in the area (Table 6). The active fault's projection to the surface is denoted by a thick line marked with "AC". Rectangles denote the rupture area. Black circles are the 2011 relocated events. Stress changes are presented on RF resolved by the average MT focal mechanisms of Table 4 and the hypocentral distribution. "Stress-loaded" or "relaxed" areas are represented in the color scale by positive or negative values, respectively. Black circles are the relocated events. Right: Coulomb stress transfer cross-sections along AB profile, parallel to the RF. The calculation depth at each panel on the left is 9 km.

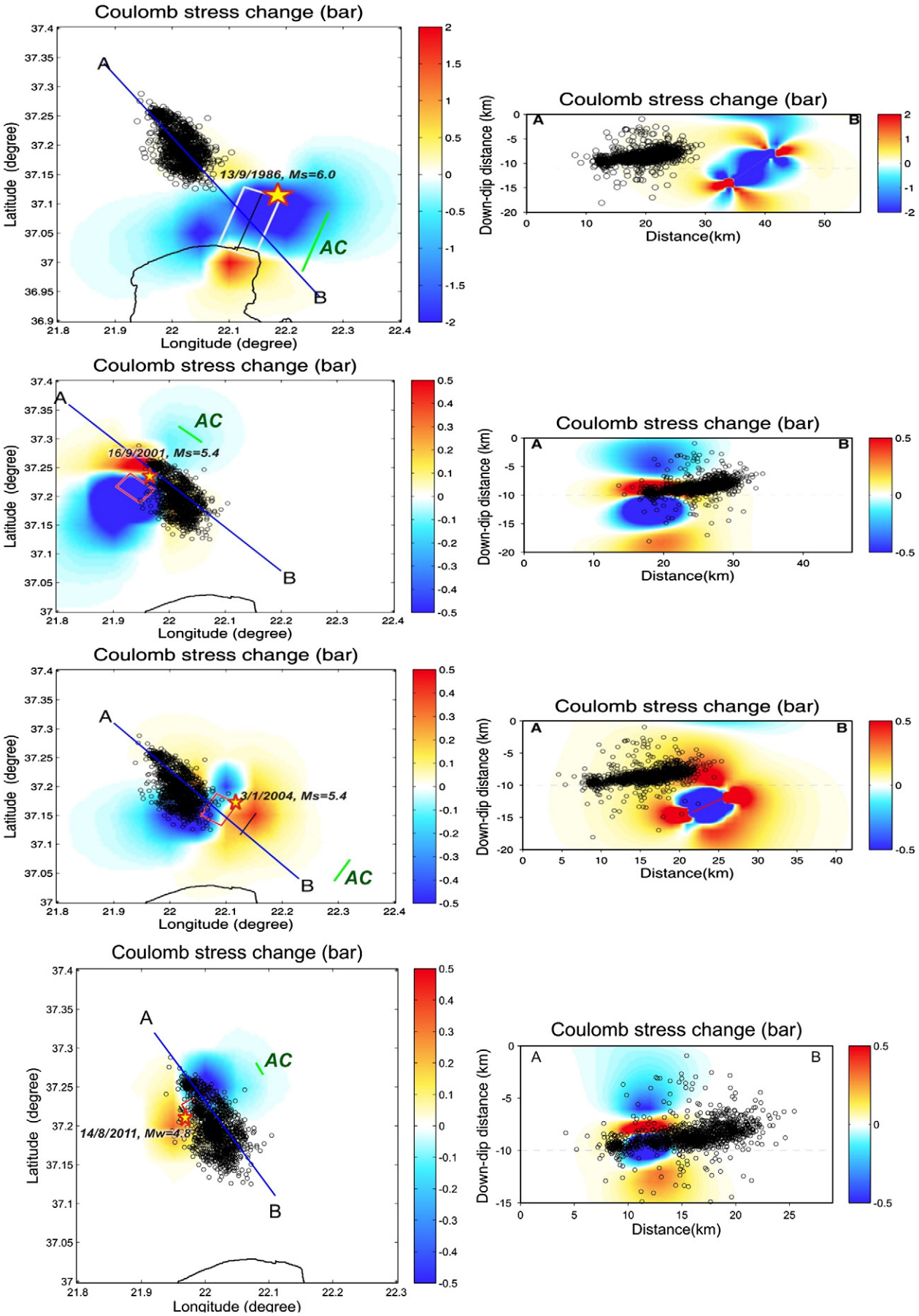
Coulomb stress change (bar)
Latitude (degree)
Longitude (degree)
A
B
AC
13/9/1986, Ms=6.0
Coulomb stress change (bar)
Down-dip distance (km)
Distance(km)
Coulomb stress change (bar)
Latitude (degree)
Longitude (degree)
A
B
AC
16/9/2001, Ms=5.4
Coulomb stress change (bar)
Down-dip distance (km)
Distance(km)
Coulomb stress change (bar)
Latitude (degree)
Longitude (degree)
A
B
AC
3/1/2004, Ms=5.4
Coulomb stress change (bar)
Down-dip distance (km)
Distance(km)
Coulomb stress change (bar)
Latitude (degree)
Longitude (degree)
A
B
AC
14/8/2011, Mw=4.8
Coulomb stress change (bar)
Down-dip distance (km)
Distance(km)

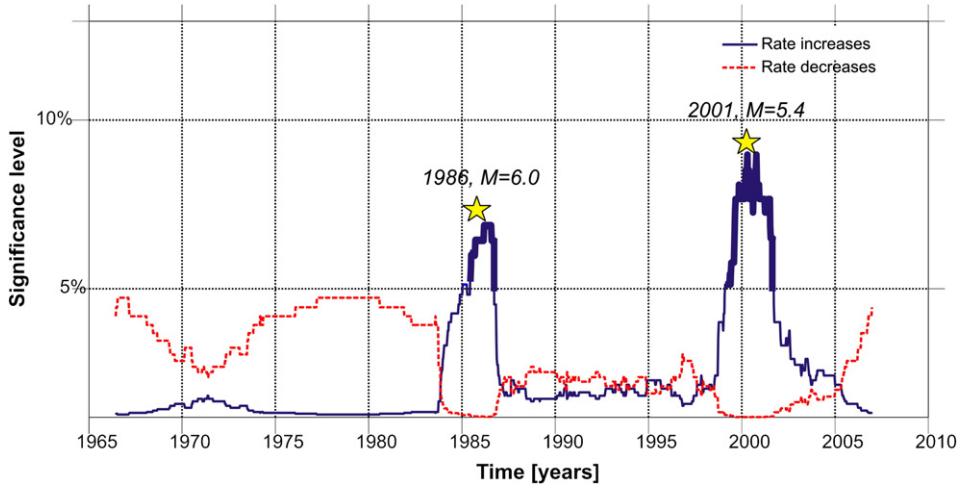

Fig. 22. Diagram showing the probability that a seismicity rate change is significant in the study area constrained within 37.1°–37.3°N, 21.9°–22.1°E, during 1964–2007 (NOA). The portions with significance >5% are drawn with thick line. The period after 2007 is not considered due to the much lower completeness magnitude compared to the period before 2007.

faults may explain both the observed ground openings at Siamo village and the inhomogeneous distribution of macroseismic intensities reported across the meizoseismal area during the activity period.

In view of the geometrical evolution of normal fault systems, the low-angle dipping configuration observed in depth is probably not continued to the surface, as normal faults tend to be concave upwards, or listric (Jackson and McKenzie, 1983). We therefore suggest that scenario B is rather probable. A similar pattern is deduced from detailed multidisciplinary investigations in the western part of the Corinth Gulf, where predominantly E–W striking and north dipping normal faults, rooting at depths of 5–12 km, overlay a low-angle detachment zone of brittle to ductile transition (Bernard et al., 1997; Chouliaras et al., 1997; Rigo et al., 1996). Given the specific common characteristics between Corinth and Upper Messinia grabens, such as their vicinity to the western Hellenic Arc and the concurrent age of initiation (about 1 My, Armijo et al., 1992), we could reasonably assume an analogous configuration between the two systems. This remark is of crucial importance for the seismic hazard of the study area and it definitely has to be considered and further clarified.

As seismicity patterns constitute effective tools to illuminate the underlying mechanisms for the generation and evolution of the earthquake swarms, we have analyzed the spatio-temporal distribution of the obtained high-resolution image of the 2011 swarm considering the following possible mechanisms: (A) Stress triggering. Stress triggering effects were studied through the Frequency–Magnitude Distribution (FMD) and the Coulomb stress transfer. (B) Fluid diffusion. It was studied through the spatio-temporal migration of hypocenters.

As the calculated FMD has shown, considerable variations of *b*-values are observed throughout the sequence, correlating well, most of the time, with the occurrence of major events. According to both *b*-value variations with time and spatial clustering of hypocenters, three phases can be distinguished during the swarm. The first phase evolved during 14/8/2011–14-9/2011, characterized by low *b*-values and hypocentral clustering mainly at the northern part. The second phase, which took place between 14/9/2011 and 12/11/2011, included several major events and is characterized by significant variations of *b*-values and migration of seismicity to the south. The last phase, during 12/11/2011–31/12/2011, presents smoother variations of *b*-values, which tend towards unity, signifying the end of the activity with a Gaussian (bell-shaped) diminution. The overall spatial distribution of *b*-values calculated from 1480 relocated events shows that the lowest ones are found in the northernmost part. Assuming that low *b*-value volumes correlate with high stress and asperities (Wiemer and Wyss, 1997), it is inferred that the northern patch of the seismogenic volume, which also hosted the largest slip, may be associated with an asperity that could be ruptured in a future earthquake. It is, however, reasonable to suspect an underlain aseismic stress relaxation mechanism that is responsible for the accumulation of effective stress and, consequently, decrease of *b*-values, related to increased pore pressure across the rupture zone. Normal to moderate *b*-values that have been found at the central and the southern patch of the fault zone correlate with seismic slip translation to the south that is compatible with earthquake cluster distribution during the second phase. Therefore, an Epidemic Type Aftershock Sequence (ETAS) model (Hainzl and Ogata, 2005), which argues that each event has a magnitude-dependent ability to trigger its own aftershocks, is inferred during this period. Differential *b*-value maps compiled for pairs of successive temporal phases, allowed the determination of areas of increased or decreased FMD rates. Small increase has been detected at the northern patch, especially during the third phase, indicating that stresses were apparently relaxed. It is noteworthy that the most significant *b*-value variations have occurred at the sites of the largest slip release.

Coulomb stress transfer computations revealed that the strongest earthquakes in the broader region did not significantly affect the 2011 epicentral area, because of the small magnitude of stress load, of the order of 0.5 bars, or less. Although, even such low stress values are capable to induce earthquakes (e.g. Stein, 1999), there is no evidence that those major events have affected the local seismic field, as no significant seismicity rate change was observed after their occurrence. We can deduce, therefore, that earthquake nucleation during 2011 can be sufficiently explained if the stress deficit is balanced by aseismic forcing (e.g. Hainzl et al., 2012). Hence, it is likely that the additional stress was induced by pore-pressure change, which critically loaded the seismogenic volume, accelerating the fault towards instability. Nevertheless, it is important to note that our analysis relied only on earthquake data. Thus, we cannot give any estimate of the total stress amplitudes, like the pre-existing shear stress. Furthermore, we have not performed any quantitative estimation of non-elastic (aseismic) processes. The explicit investigation of those processes would require additional observational constraints and assumptions, which are beyond our scope. It is noteworthy, however, that Kyriakopoulos et al. (2013) have found a difference between seismic and geodetic moments for the interval 3/7–1/10/2011 in the epicentral area, suggesting an ongoing region-wide aseismic creep over the same period.

Fluid diffusion is reflected in the spatio-temporal hypocenter migration. Seismicity spreading can be often modeled by pore-pressure

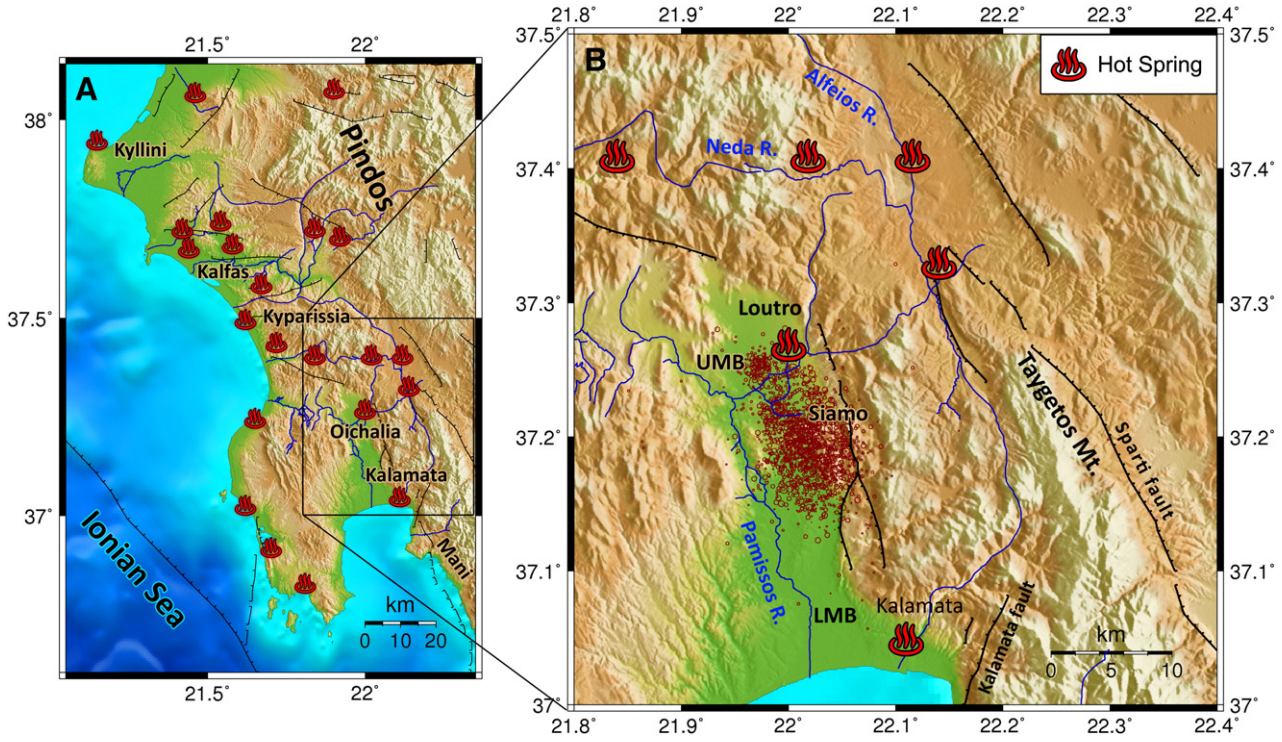

Fig. 23. A) Map showing the location of the known hot springs (see the corresponding symbols) in western Peloponnesus (after Kiskyras, 1962). Black barbed lines are scarps of normal faults after Armijo et al. (1992) and Lyon-Caen et al. (1988). Open circles represent the relocated epicenters of the 2011 seismic swarm. Continuous curves denote the main hydrographic network along with the names of certain rivers. B) Zoom-in map corresponding to the box of the left panel. UMB: Upper Messinia Basin. LMB: Lower Messinia Basin.

diffusion (Shapiro et al., 1997). In this case, earthquakes are representing localized shear fracturing, due to incremental changes of the effective load rather than expressing an ongoing larger fracturing (Cornet et al., 2007). We found that the spatio-temporal hypocenter migration is bounded by the theoretical curve of the triggering front (Eq. (2)) with hydraulic diffusivity $D \approx 1.10$ m^2/s, supposing that the fluid intrusion event started 6 days before the major shock of August 14th, in the vicinity of its hypocenter. However, the occurrence of several events at the northernmost part of the swarm during June–July 2011, points towards external triggering, most probably due to injection of pressurized fluids that could have started more than a month before the major event. The average rate of the seismicity migration towards the south during the first 80 days was found at about 80 m/day. At the same time, the diffusion appears to ascend to shallower depths towards the southern part. In the scientific literature, similar methodology has been followed in many cases for the interpretation of seismicity caused by fluids intrusion, with a wide range of D values from the order of 10^{-2} m^2/s up to a few m^2/s, measured using the triggering front parabolic envelope (e.g. Kraft et al., 2006; Liu et al., 2013; Pacchiani and Lyon-Caen, 2010; Rigo, 2010).

Summarizing, in the Oichalia earthquake swarm region crustal fluids likely play a key role in the alteration of the pre-existing faults from subcritical to critical state, due to pore pressure increase. After bringing the fault to instability, the swarm activity is mainly driven by the stress changes due to co-seismic and post-seismic slips, which considerably depend on the frictional conditions at the fault. According to the relocated spatio-temporal distribution, the swarm was initiated north of Oichalia, beneath the Loutro sulfide thermal spring (Fig. 23) and propagated towards the SSE, at a rate of ~80 m/day (Fig. 15). The clustering analysis, showed that the swarm evolved in three major phases, employing fluids and ETAS. As deduced from the Coulomb stress transfer that was induced by past major earthquakes in the region, which did not cause any significant post-seismic rate increase, the stress deficit area, certainly requires external triggering, which may be attributed to fluid injection. After the fault patch was brought into a critical state by increase of the pore pressure, the swarm was further driven by self-organization due to stress transfer. The second phase, during 14/9/2011–12/11/2011, started with the occurrence of a major earthquake on September 14th, likely triggered by another fluid injection and possibly followed by afterslip due to ambient stress redistribution. Thereafter, the last phase produced increased activity at the northern part, relaxing the stressed area and driving it into post-seismic balance.

Several mineral thermal springs that have been reported in the broader region of western Peloponnesus since the antiquity (Fig. 23) are classified as “relatively hot–hot springs” (Kappelmeyer and Haenel, 1974; Lambrakis and Kallergis, 2005) and attributed to indigenous heat (Stratikopoulos, 2007). Their existence typically implies for increased crustal fluids of meteoric or marine origin circulating in depth. If this is the case that smaller scale conjugate faults rooting at depth dominate the seismogenic volume, forming the inferred from seismicity low-angle seismic zone, these likely enhance fluid circulation through the weakened crust. The results of our analysis converge towards the involvement of crustal fluids that contribute to earthquake triggering by imposing decrease of the effective friction coefficient. However, in order to evaluate our assessment on the fluid aspect, additional experimental constraints are required complementary to the seismic data, towards the quantification of underlying non-tectonic forcing processes, that is by implementing CGPS measurements and a 3-D seismic tomography study.

Acknowledgments

This research was partly financed by the XENIOS Project (09ΣΥΝ-31-867), coordinated by the Greek Ministry of Research and Technology and the LACAE, Faculty of Geology and Geoenvironment, NKUA. It was also partially funded by SARG-UoA. We are grateful to the Administration of Peloponnesus and Local Authorities. We are thankful to the two anonymous reviewers for their critical comments, which largely contributed to the improvement of the manuscript. Most figures were drawn using the GMT software (Wessel and Smith, 1995).

References

Armijo, R., Lyon-Caen, H., Papanastassiou, D., 1992. East–west extension and Holocene normal-fault scarps in the Hellenic Arc. Geology 20 (6), 491–494. http://dx.doi.org/10.1130/0091-7613.

Bender, B., 1983. Maximum likelihood estimation of b-values for magnitude grouped data. Bull. Seismol. Soc. Am. 73, 831–851.

Bernard, P., Briole, P., Meyer, B., Lyon-Caen, H., Gomez, J.-M., Tiberi, C., Berge, C., Cattin, R., Hatzfeld, D., Lachet, C., Lebrun, B., Deschamps, A., Courboulex, F., Larroque, C., Rigo, A., Massonnet, D., Papadimitriou, P., Kassaras, J., Diagourtas, D., Makropoulos, K., Veis, G., Papazisi, E., Mitsakaki, C., Karakostas, V., Papadimitriou, E., Papanastassiou, D., Chouliaras, M., Stavrakakis, G., 1997. The Ms = 6.2, June 15,1995 Aigion earthquake (Greece): evidence for low-angle normal faulting, in the Corinth rift. J. Seismol. 1, 131–150.

Chouliaras, G., Pham, V.N., Boyer, D., Bernard, P., Stavrakakis, G.N., 1997. Crustal structure of the Gulf of Corinth in Central Greece from magnetotelluric soundings. Ann. Geophys. XL (1), 61–67.

Chouliaras, G., Drakatos, G., Pavlou, K., Makropoulos, K., 2013. Stress distribution and seismicity patterns of the 2011 seismic swarm in the Messinia basin, (South-Western Peloponnesus), Greece. Nat. Hazards Earth Syst. Sci. 13, 45–51.

Cornet, F.H., Berard, T., Bourouis, S., 2007. How close to failure is a granite rock at a 5 km depth? Int. J. Rock Mech. Min. Sci. 44, 47–66.

Crosson, R.S., 1976. Crustal structure modeling of earthquake data; 1, Simultaneous least squares estimation of hypocenter and velocity parameters. J. Geophys. Res. 81, 3036–3046.

Drakatos, G., Melis, N., Papanastassiou, D., Karastathis, V., Papadopoulos, G., Stavrakakis, G., 2002. 3-D crustal velocity structure from inversion of local earthquake data in Attiki (Central Greece) region. Nat. Hazards 27, 1–14.

Efron, B., 1982. The Jacknife, the Bootstrap, and Other Resampling Plans. SIAM, Philadelphia (92 pp.).

Efron, B., Tibshirani, R.J., 1993. An Introduction to the Bootstrap. Chapman and Hall, New York.

Floyd, M.A., Billiris, H., Paradissis, D., Veis, G., Avallone, A., Briole, P., McClusky, S., Nocquet, J.-M., Palamartchouk, K., Parsons, B., England, P.C., 2010. A new velocity field for Greece: implications for the kinematics and dynamics of the Aegean. J. Geophys. Res. 115, B10403. http://dx.doi.org/10.1029/2009JB007040.

Fytrolakis, N., 1971. Geological studies in Pylia province (Messinia, Peloponessus, Greece). (Ph.D. Thesis) Ann. Geol. Des Pays Hellen, 23, pp. 57–122 (in Greek with German abstract).

Ganas, A., Parsons, T., 2009. Three-dimensional model of Hellenic Arc deformation and origin of the Cretan uplift. J. Geophys. Res. 114, B06404. http://dx.doi.org/10.1029/2008JB005599.

Ganas, A., Lekkas, E., Kolligri, M., Moshou, A., Makropoulos, K., 2012. The 2011 Oichalia (SW Peloponnesus, Greece) seismic swarm: geological and seismological evidence for E–W extension and reactivation of the NNW–SSE normal fault. Bull. Geol. Soc. Greece XLVI, 81–94.

Grünthal, G., 1998. European Macroseismic Scale 1998 (EMS-98). Cahiers du Centre Européen de Géodynamique et de Séismologie 15. Centre Européen de Géodynamique et de Séismologie, Luxembourg (99 pp.).

Gutenberg, B., Richter, C.F., 1944. Frequency of earthquakes in California. Bull. Seismol. Soc. Am. 34, 185–188.

Hainzl, S., Ogata, Y., 2005. Detecting fluid signals in seismicity data through statistical modelling. J. Geophys. Res. 110 (B05), S07. http://dx.doi.org/10.1029/2004JB003247.

Hainzl, S., Fischer, T., Dahm, T., 2012. Seismicity-based estimation of the driving fluid pressure in the case of swarm activity in Western Bohemia. Geophys. J. Int. 191, 271–281.

Haslinger, F., Kissling, E., Ansorge, J., Hatzfeld, D., Papadimitriou, E., Karakostas, V., Makropoulos, K., Kahle, H.-G., Peter, Y., 1999. 3D crustal structure from local earthquake tomography around the Gulf of Arta (Ionian region, NW Greece). Tectonophysics 304, 201–218.

Hatzfeld, D., Pedotti, G., Hatzidimitriou, P., Makropoulos, K., 1990. The strain pattern in the western Hellenic arc deduced from a microearthquake survey. Geophys. J. Int. 101, 181–202.

Heinloo, A., Trabant, C., 2004. SeisComP 2.1 Manual. 35 (http://www.gfz-potsdam.de/geofon/new/scp.html).

Hill, D.P., 1977. A model for earthquake swarms. J. Geophys. Res. 82, 1347–1352.

Horálek, J., Fischer, T., 2008. Role of crustal fluids in triggering the West Bohemia/Vogtland earthquake swarms. Just what we know (a review). Stud. Geophys. Geod. 52, 455–478.

Ibs-von Seht, M., Plenefisch, T., Klinge, K., 2008. Earthquake swarms in continental rifts — a comparison of selected cases in America, Africa and Europe. Tectonophysics 452, 66–77.

Jackson, J., McKenzie, D., 1983. The geometrical evolution of normal fault systems. J. Struct. Geol. 5 (5), 471–482.

Jackson, J.A., McKenzie, D., 1984. Active tectonics of the Alpine–Himalayan Belt between western Turkey and Pakistan. Geophys. J. Int. 77 (1), 185–264. http://dx.doi.org/10.1111/j.1365-246X.1984.tb01931.x.

Kagan, Y., 1999. Universality of the seismic moment–magnitude relation. Pure Appl. Geophys. 155, 537–574.

Kapetanidis, V., Papadimitriou, P., 2011. Estimation of arrival-times in intense seismic sequences using a Master-Events methodology based on waveform similarity. Geophys. J. Int. 187, 889–917. http://dx.doi.org/10.1111/j.1365-246X.2011.05178.x.

Kapetanidis, V., Papadimitriou, P., Makropoulos, K., 2010. A cross-correlation technique for relocation of seismicity in the western Corinth rift. Proc. of the 12th International Congress, Patras, May 2010. Bull. Geol. Soc. Greece, XLIII, No 4, pp. 2015–2025.

Kappelmeyer, O., Haenel, R., 1974. Geothermics with special reference to application. Geoexploration Monographs, Series 1, No. 4. Gebrueder Borntraeger, Berlin (251 pp.).

Karagianni, E.E., Papazachos, C.B., Panagiotopoulos, D.G., Suhaldoc, P., Vuan, A., Panza, G.F., 2005. Shear velocity structure in the Aegean area obtained by inversion of Rayleigh waves. Geophys. J. Int. 160, 127–143.

Kennett, B.N.L., 1983. Seismic Wave Propagation in Stratified Media. Cambridge University Press, Cambridge.

King, G.C.P., Stein, R.S., Lin, J., 1994. Static stress changes and the triggering of earthquakes. BSSA 84 (3), 935–953.

Kiskyras, D.A., 1962. The mineral springs of Peloponnesus. Peloponnesian New Years. 103–109.

Kisslinger, C., 1975. Processes during the Matsushiro swarm as revealed by leveling, gravity, and spring-flow observations. Geology 3, 57–62.

Klein, F.W., 1989. HYPOINVERSE, a program for VAX computers to solve for earthquake locations and magnitudes. U.S. Geological Survey Open-File Report, pp. 89–314 (59 pp.).

Kraft, T., Wassermann, J., Schmedes, E., Igel, H., 2006. Meteorological triggering of earthquake swarms at Mt. Hochstaufen, SE-Germany. Tectonophysics 424, 245–258.

Kyriakopoulos, C., Chini, M., Bignami, C., Stramondo, S., Ganas, A., Kolligri, M., Moshou, A., 2013. Monthly migration of a tectonic seismic swarm detected by DInSAR: southwest Peloponnese, Greece. Geophys. J. Int.. http://dx.doi.org/10.1093/gji/ggt196.

Ladas, I., Mariolakos, I., Fountoulis, I., 2004. Neotectonic deformation of Eastern Pylia (SW Peloponnesus, Greece). Bull. Geol. Soc. Greece 36, 1652–1661.

Lambrakis, N., Kallergis, G., 2005. Contribution to the study of Greek thermal springs: hydrogeological and hydrochemical characteristics and origin of thermal waters. Hydrogeol. J. 13, 506–521.

Lay, T., Wallace, T.C., 1995. Modern Global Seismology. Academic Press, San Diego.

Le Pichon, X., 1983. Land-locked oceanic basins and continental collision: the Eastern Mediterranean as a case example. In: Hsu, K.J. (Ed.), Mountain Building Processes. Academic, London, pp. 201–211.

Liu, Y., Chen, T., Xie, F., Dub, F., Yang, D., Zhang, L., Xua, L., 2013. Analysis of fluid induced aftershocks following the 2008 Wenchuan M_s 8.0 earthquake. Tectonophysics 2013. http://dx.doi.org/10.1016/j.tecto.2013.09.010.

Lyon-Caen, H., Armijo, R., Drakopoulos, J., Baskoutas, J., Delibassis, N., Gaulon, R., Kouskouna, V., Latoussakis, J., Makropoulos, K., Papadimitriou, P., Papanastassiou, D., Pedotti, G., 1988. The 1986 Kalamata (South Peloponnesus) earthquake: detailed study of a normal fault, evidences for east–west extension in the Hellenic Arc. J. Geophys. Res. 93 (B12), 14967–15000. http://dx.doi.org/10.1029/JB093iB12p14967.

Lyon-Caen, H., Papadimitriou, P., Deschamps, A., Bernard, P., Makropoulos, K., Pacchiani, F., Patau, G., 2004. First results of the CRLN seismic network in the Western Corinth Rift: evidence for old-fault reactivation. C. R. Geosci. 336, 343–351.

Main, I.G., 1996. Statistical physics, seismogenesis, and seismic hazard. Rev. Geophys. 34, 433–462.

Makropoulos, K., Kaviris, G., Kouskouna, V., 2012. An updated and extended earthquake catalogue for Greece and adjacent areas since 1900. Nat. Hazards Earth Syst. Sci. 12, 1425–1430.

Mariolakos, I., Fountoulis, I., Marcopoulou-Diacantoni, A., Mirkou, M.R., 1994. Some remarks on the kinematic evolution of Messinia Province (SW Peloponnesus, Greece) during the Pleistocene based on neotectonic stratigraphic and paleoecological observations. Munster. Forsch. Geol. Palaont. 76, 371–380 (Munster).

McClusky, S., Balassanian, S., Barka, A., Demir, C., Ergintav, S., Georgiev, I., Gurkan, O., Hamburger, M., Hurst, K., Kahle, H., Kastens, K., Kekelidze, G., King, R., Kotzev, V., Lenk, O., Mahmoud, S., Mishin, A., Nadariya, M., Ouzounis, A., Paradissis, D., Peter, Y., Prilepin, M., Reilinger, R., Sanli, I., Seeger, H., Tealeb, A., Toksöz, M.N., Veis, G., 2000. Global Positioning System constraints on plate kinematics and dynamics in the eastern Mediterranean and Caucasus. J. Geophys. Res. 105 (B3), 5695–5719. http://dx.doi.org/10.1029/1999JB900351.

McKenzie, D.P., 1969. The relation between fault plane solutions for earthquakes and the directions of the principal stresess. BSSA 59, 591–601.

McKenzie, D., 1972. Active tectonics of the Mediterranean region. Geophys. J. R. Astron. Soc. 30, 109–185.

Mogi, K., 1963. Some discussions on aftershocks, foreshocks and earthquake swarms — the fracture of a semi-infinite body caused by an inner stress origin and its relation to the earthquake phenomena. Bull. Earthq. Res. Inst. Tokyo Univ. 41, 615–658.

Noir, J., Jacques, E., Bekri, S., Adler, P.M., Tapponnier, P., King, G.C.P., 1997. Fluid flowtriggered migration of events in the 1989 Dobi earthquake sequence of Central Afar. Geophys. Res. Lett. 24, 2335–2338.

Novotny, O., Zahradnik, J., Tselentis, G.A., 2001. Northwestern Turkey earthquakes and the crustal structure inferred from surface waves observed in western Greece. Bull. Seismol. Soc. Am. 91, 875–879.

Nyst, M., Thatcher, W., 2004. New constraints on the active tectonic deformation of the Aegean. J. Geophys. Res. 109, B11406. http://dx.doi.org/10.1029/2003JB002830.

Pacchiani, F., Lyon-Caen, H., 2010. Geometry and spatio-temporal evolution of the 2001 Agios Ioanis earthquake swarm (Corinth Rift, Greece). Geophys. J. Int. 180, 59–72. http://dx.doi.org/10.1111/j.1365-246X.2009.04409.x.

Papazachos, C.B., Nolet, G., 1997. P and S velocity structure of the Hellenic area obtained by robust nonlinear inversion of travel times. J. Geophys. Res. 102 (8), 349–367.

Papazachos, B., Papazachou, C., 2003. Earthquakes of Greece, 3rd edition. Ziti Publications, Thessaloniki (286 pp.).

Papazachos, B.C., Karakostas, V.G., Papazachos, C.B., Scordilis, E.M., 2000. The geometry of the Wadati-Benioff zone and lithospheric kinematics in the Hellenic Arc. Tectonophysics 319 (4), 275–300. http://dx.doi.org/10.1016/S0040-1951(99)00299-1.

Papoulia, J., Makris, J., 2004. Microseismicity and active deformation of Messinia, SW Greece. J. Seismol. 8, 439–451.

Pavlides, S., 1993. Active faulting in multi-fractured seismogenic areas; examples from Greece. Z. Geomorphol. N.F. 57–72.

Pollitz, F.F., Sacks, I.S., 1992. Modeling of postseismic relaxation following the great 1857 earthquake, southern California. Bull. Seismol. Soc. Am. 82, 454–480.
Randall, G.E., 1994. Efficient calculation of complete differential seismograms for laterally homogeneous earth models. Geophys. J. Int. 118, 245–254.
Rigo, A., 2010. Precursors and fluid flows in the case of the 1996, ML = 5.2 Saint-Paul-de-Fenouillet earthquake (Pyrenees, France): a complete pre-, co- and post-seismic scenario. Tectonophysics 480 (2010), 109–118.
Rigo, A., Lyon-Caen, H., Armijo, H.R., Deschamps, A., Hatzfeld, D., Makropoulos, K., Papadimitriou, P., Kassaras, I., 1996. A microseismic study in the western part of the Gulf of Corinth (Greece): implications for large scale normal faulting mechanisms. Geophys. J. Int. 126, 663–688.
Roberts, G.P., Ganas, A., 2000. Fault-slip directions in central and southern Greece measured from striated and corrugated fault planes: comparison with focal mechanism and geodetic data. J. Geophys. Res. 105 (23), 443–462. http://dx.doi.org/10.1029/1999JB900440.
Roumelioti, Z., Benetatos, Ch., Kiratzi, A., 2009. The 14 February 2008 earthquake (M6.7) sequence offshore south Peloponnesus (Greece): source models of the three strongest events. Tectonophysics 387, 65–79.
Schoenball, M., Muller, T.M., Muller, B.I.R., Heidbach, O., 2010. Fluid-induced microseismicity in pre-stressed rock masses. Geophys. J. Int. 180, 813–819. http://dx.doi.org/10.1111/j.1365-246X.2009.04443.x.
Scholz, C.H., 1968. The frequency–magnitude relation of microfracturing in rock and its relation to earthquakes. Bull. Seismol. Soc. Am. 58, 399–415.
Scholz, C.H., 2002. The Mechanics of Earthquakes and Faulting, 2nd ed. Cambridge Univ. Press, New York (471 pp.).
Schorlemmer, D., Wiemer, S., Wyss, M., 2005. Variation in earthquake-size distribution across different stress regimes. Nature 437, 539–542.
Shapiro, S.A., Huenges, E., Borm, G., 1997. Estimating the crust permeability from fluid-injection-induced seismic emission at the KTB site. Geophys. J. Int. 131, 15–18.
Shi, Y., Bolt, B.A., 1982. The standard error of the magnitude–frequency b-value. Bull. Seismol. Soc. Am. 72, 1677–1687.
Stein, R.S., 1999. The role of stress transfer in earthquake occurrence. Nature 605–609. http://dx.doi.org/10.1038/45144.
Stratikopoulos, K., 2007. Hydrogeological and Hydrochemical of the Thermal Mineral Water Springs of Western Peloponnesus, With the Use of Steady Isotopes. (MSc Thesis) University of Patras (88 pp.).
Taymaz, T., Jackson, J.A., Westaway, R., 1990. Earthquake mechanisms in the Hellenic Trench near Crete. Geophys. J. Int. 102, 695–731. http://dx.doi.org/10.1111/j.1365-246X.1990.tb04590.x.
Toda, S., Stein, R.S., Sevilgen, V., Lin, J., 2011. Coulomb 3.3 graphic-rich deformation and stress-change software for earthquake, tectonic, and volcano research and teaching—user guide. U.S. Geological Survey Open-File Report 2011-1060 (63 pp.).
Vernant, P., Reilinger, R., McClusky, S., 2014. Geodetic evidence for low coupling on the Hellenic subduction plate interface. Earth Planet. Sci. Lett. 385, 122–129. http://dx.doi.org/10.1016/j.epsl.2013.10.018.
Waldhauser, F., 2001. HypoDD: a computer program to compute double-difference earthquake locations. U.S. Geol. Surv. Open-File Report, 01-113, Menlo Park, California.
Waldhauser, F., Ellsworth, W.L., 2000. A double-difference earthquake location algorithm: method and application to the northern Hayward fault. Bull. Seismol. Soc. Am. 90, 1353–1788.
Waldhauser, F., Richards, P.G., 2004. Reference events for regional seismic phases at IMS stations in China. Bull. Seismol. Soc. Am. 94 (6), 2265–2279.
Wessel, P., Smith, W., 1995. New version of the Generic Mapping Tools. EOS 76-329.
Westerhaus, M., Wyss, M., Yilmaz, R., Zschau, J., 2002. Correlating variations of b-values and crustal deformations during the 1990s may have pinpointed the rupture initiation of Mw = 7.4 Izmit earthquake of 1999 August 17. Geophys. J. Int. 148, 139–152.
Wiemer, S., 1996. ZMAP Users Guide, Version 3.0. Geophysical Institute, University of Alaska, Fairbanks.
Wiemer, S., 2001. A software package to analyze seismicity: ZMAP. Seismol. Res. Lett. 72, 374–383.
Wiemer, S., Benoit, J., 1996. Mapping the b-value anomaly at 100 km depth in the Alaska and New Zealand subduction zones. Geophys. Res. Lett. 23, 1557–1560.
Wiemer, S., Katsumata, K., 1999. Spatial variability of seismicity parameters in aftershock zones. J. Geophys. Res. 104, 13,135–13,151.
Wiemer, S., Wyss, M., 1997. Mapping the frequency–magnitude distribution in asperities: an improved technique to calculate recurrence times? J. Geophys. Res. 102 (B7), 15 115–15 128.
Wiemer, S., Wyss, M., 2002. Mapping spatial variability of the frequency–magnitude distribution of earthquakes. Adv. Geophys. 45, 259–302.
Wilcock, W.S.D., 2012. Tracking fin whales in the northeast Pacific Ocean with a seafloor seismic network. J. Acoust. Soc. Am. 132, 2408. http://dx.doi.org/10.1121/1.4747017.
Wyss, M., 1973. Towards a physical understanding of the earthquake frequency distribution. Geophys. J. R. Astron. Soc. 31, 341–359.
Wyss, M., Shimazaki, K., Wiemer, S., 1997. Mapping active magma chambers by b values beneath the off-Ito volcano, Japan. J. Geophys. Res. 102 (B9), 20413–20422.
Yamashita, T., 1999. Pore creation due to fault slip in a fluid-permeated fault zone and its effect on seismicity: generation mechanism of earthquake swarm. Pure Appl. Geophys. 155, 625–647.